Strain- and Defect-Mediated Thermal Conductivity in Silicon Nanowires

Kathryn F. Murphy,[†] Brian Piccione,[†] Mehdi B. Zanjani,[‡] Jennifer R. Lukes,[‡] and Daniel S. Gianola*,[†,‡]

[†]Department of Materials Science and Engineering and [‡]Department of Mechanical Engineering and Applied Mechanics, University of Pennsylvania, Philadelphia, Pennsylvania 19104, United States

S *Supporting Information*

ABSTRACT: The unique thermal transport of insulating nanostructures is attributed to the convergence of material length scales with the mean free paths of quantized lattice vibrations known as phonons, enabling promising next-generation thermal transistors, thermal barriers, and thermo-electrics. Apart from size, strain and defects are also known to drastically affect heat transport when introduced in an otherwise undisturbed crystalline lattice. Here we report the first experimental measurements of the effect of both spatially uniform strain and point defects on thermal conductivity of an individual suspended nanowire using in situ Raman piezothermography. Our results show that whereas phononic transport in undoped Si nanowires with diameters in the range of 170−180 nm is largely unaffected by uniform elastic tensile strain, another means of disturbing a pristine lattice, namely, point defects introduced via ion bombardment, can reduce the thermal conductivity by over 70%. In addition to discerning surface- and core-governed pathways for controlling thermal transport in phonon-dominated insulators and semiconductors, we expect our novel approach to have broad applicability to a wide class of functional one- and two-dimensional nanomaterials.

KEYWORDS: *Silicon nanowire, thermal conductivity, Raman, defect, strain, roughness*
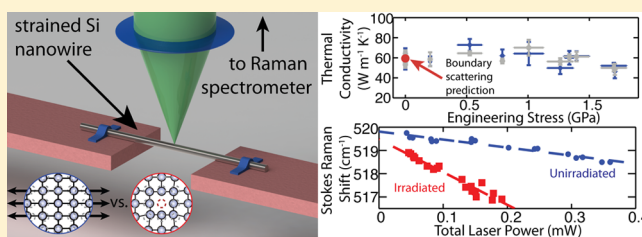
A fundamental problem facing the rational design of new materials is the independent control of electrical and thermal properties with implications for a wide range of applications including thermoelectrics,[1,2] flexible electronics,[3] solar thermal electricity generation[4] or carbon capture,[5] and thermal logic.[6] One strategy for controlling transport involves manipulating the length scales that affect it. For instance, the thermoelectric figure of merit in Si increases by orders of magnitude in nanowire or thin film form; this arises from a lowering of thermal conductivity with relatively little change in electrical properties when the confining dimension (e.g., nanowire diameter) is small enough that a significant fraction of phonons are scattered at free surfaces.[7,8] However, tailoring properties by geometry or chemistry alone limits the range of achievable thermal conductivities and furthermore does not allow for on-demand modification of transport, precluding applications that require responsive behavior such as thermal transistors;[9] thermoelectric modules that adapt to their environmental temperature in order to maximize efficiency; or switchable thermal barriers for heat management.

One means of reversibly and adaptively tuning transport is elastic strain, which has long been known to strongly affect electronic band structure and has been successfully exploited to improve carrier mobility in electronic devices.[10] Simulations point to a lowering of thermal conductivity with tensile strain due to changes in phonon frequencies and unit cell volume, which result in altered heat capacity, velocity, and mean free path.[11−14] Strain arising from heteroepitaxial interfaces can

yield increased phonon scattering due to the atomic interfacial misfit,[15] and superlattices comprising alternating thin films[16−18] have exhibited lowered thermal conductivity compared to the alloy limit. Another means of controlling thermal transport is by the introduction or removal of crystalline defects such as vacancies, impurities, or dislocations, which strongly modify phonon scattering,[19−23] as has been experimentally observed for InAs nanowires[24] and bulk SiC[25,26] and InN.[27] Such defects may serve to affect phonon scattering times through local changes in mass (or absence of atoms in the case of vacancies), interatomic bonding forces, and strain gradients in the vicinity of the defect. Nanowires are ideal for the study of both uniform strain and defect effects due to the availability of a range of elastic strain an order of magnitude larger than in bulk[28,29] and because controlled defect densities can be introduced in a relatively large fraction of the sample volume as compared with surface treatments (e.g., irradiation or diffusive processes) of bulk materials.

The lack of experimental measurements of strain-mediated thermal conductivity is largely due to the complexity of simultaneously applying and measuring stress or strain, heating, and measuring temperature. One versatile, noncontact method of measuring thermal conductivity is Raman thermography,[30] which uses a laser to heat a suspended specimen and the
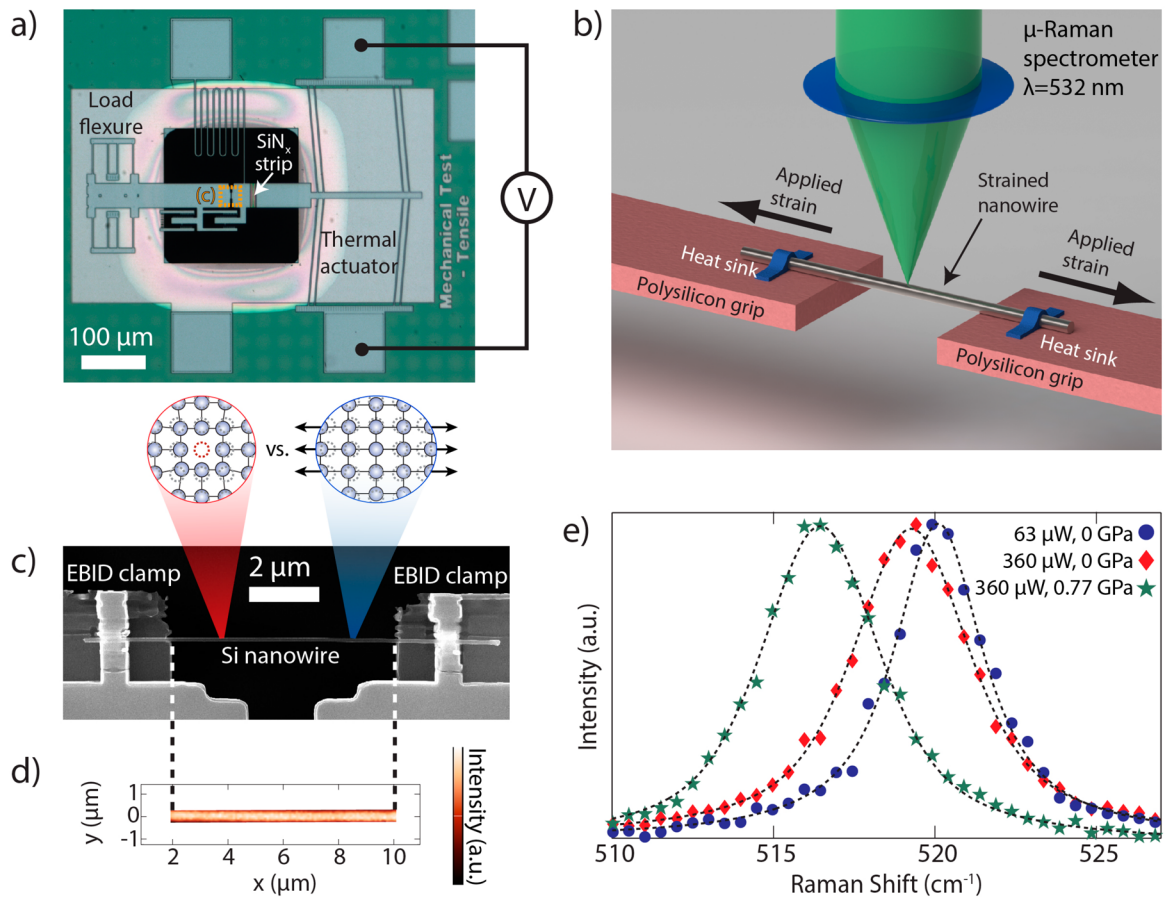
Figure 1. In situ Raman piezothermography method applied to strained, suspended nanowires. (a) Optical image of the MEMS tensile testing device. When current is run through the thermal actuator, the angled beams Joule heat and expand, pulling apart the grips. Load is determined by measuring the deflection of the compound flexure load cell. (b) Schematic of experimental setup. (c) SEM image of a $\langle 111 \rangle$ Si nanowire clamped to the MEMS device. (d) A to-scale map of Raman peak intensities. (e) Sample spectra collected at low (63 μW) and high (360 μW) applied laser powers (equivalently, low and high temperature) and at zero and 0.77 GPa of stress. Dotted lines are fits to Gaussian + Lorentzian line shape.

spectrum of inelastically scattered light to measure temperature. Raman additionally provides information on phonon frequencies and densities of states, making it particularly well-suited to studying phonon transport. This noncontact method has been successfully applied to stress-free nanostructures such as cantilevered SiNWs,[31] bridged GaAs nanowires,[32] bridged carbon nanotubes,[33,34] bridged graphene,[30,35−37] and suspended MoS$_2$.[38] However, the difficulty of decoupling the effects of strain or high defect densities from temperature on the frequencies of the Raman-active modes has largely prevented this method from being used on strained or defected samples.

In this work, we present the first study of the coupling between thermal conductivity and both elastic strain and point defects in the same nanostructure using a novel method that we dub Raman piezothermography. We mount an individual Si nanowire on a microelectromechanical system (MEMS)-based tensile testing device and apply controlled, uniaxial tensile strain over an order of magnitude higher than can be achieved in bulk Si. To explore the effect of point defects, we lightly irradiated the same wire (as well as two others of similar size and shape) to introduce vacancies, self-interstitials, and implanted impurities that introduce phonon scattering sites that reside in the core of the nanowire and not at the free surface. Our results show that such defects are far more effective at lowering thermal conductivity than uniform strain,

suggesting new strategies for tunable thermal conductivity. By examining two distinct defect states in a single nanowire, we furthermore provide evidence that core defects play a drastically larger role in reducing thermal conductivity than surface roughening, contrary to suggestions from recent experiments.

The total thermal resistance of a system may be written in terms of the Raman shift ω and absorbed laser power P as[35,39]

$$R_{\text{system}} = \frac{\partial T}{\partial P} = \frac{1}{\chi_T} \frac{\partial \omega}{\partial P} \tag{1}$$

where χ_T is the relationship between first-order Raman shift and temperature for Si nanowires ($\chi_T = \partial \omega / \partial T = -0.022$ cm^{-1}[40]). Equation 1 yields the total thermal resistance of the system, including the effects of contact resistance and air conduction. In order to distinguish these effects from the thermal conductivity of the sample, we make use of the fact that the temperature rise in a suspended nanostructure will be a function of the thermal resistances of all components of the thermal system. We therefore scan a point source, a laser, along a doubly clamped specimen such that the shape of the resulting heating profile, as measured at the source, is a signature of the thermal resistances of the components of the system. Solving the heat equation for a suspended, doubly clamped, quasi-1D system heated with a pointlike power source of magnitude P, the temperature rise ΔT at the power source as a function of source position x is given by
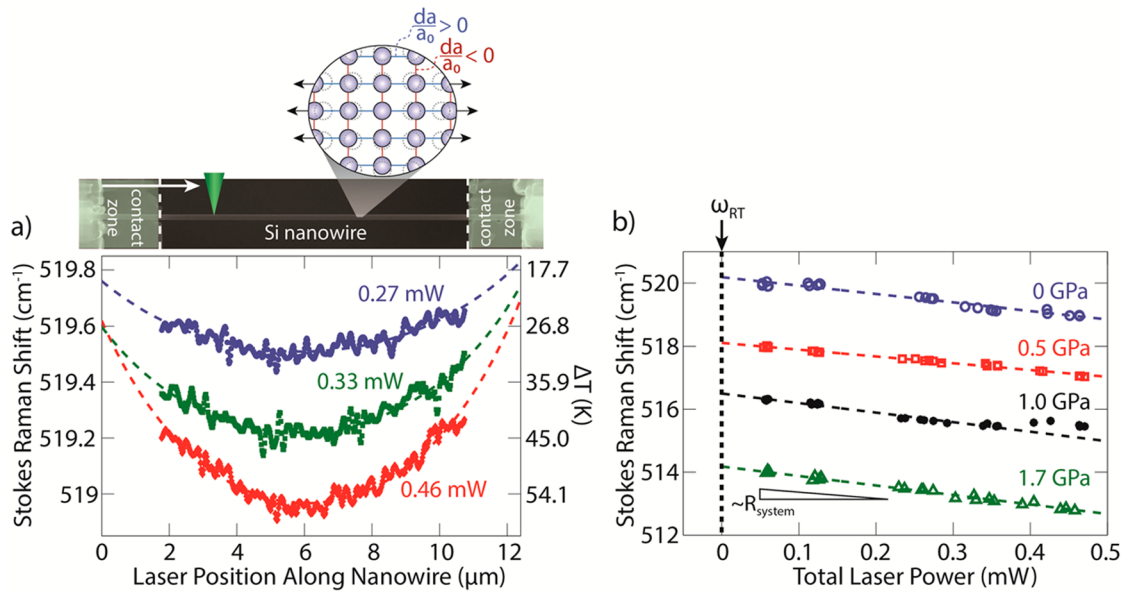
Figure 2. Self-consistent approach for determining thermal conductivity of a strained nanowire. (a) Raman shift as a function of laser position along the nanowire. Spatially resolved spectra were collected with a 100 nm step, and the maps of peak intensity and position were interpolated with 20 nm spacing. As laser power increases, temperature increases, resulting in an overall downshift of the curves. The concave shape is due to the thermal resistance of the wire, heat losses to air, and the contacts with the heat sinks on either end. Residuals of the fits are shown in the Supporting Information. (b) The minima of the fits shown in (a) for each laser intensity for several increments of stress. The slope of this curve is the total thermal resistance of the system, and the zero-intercept of the fit is taken to be the room-temperature peak position. Determination of the room-temperature peak position allows us to plot temperature as a function of peak position (secondary axis of (a)) for any strain.

$$\Delta T(x) = P \frac{[MR_{c,r} \cosh(m(L-x)) + \sinh(m(L-x))][MR_{c,l} \cosh(mx) + \sinh(mx)]}{M[M(R_{c,l} + R_{c,r})\cosh(mL) + (1 + M^2 R_{c,l} R_{c,r})\sinh(mL)]}$$

(2)

where $M \equiv (ChA\kappa)^{1/2}$ and $m \equiv [(Ch)/(A\kappa)]^{1/2}$. Here L is the length of the nanowire; A is its cross-sectional area; C is its circumference; κ is the material thermal conductivity (comprising both electronic and phononic components); $R_{c,l}$ and $R_{c,r}$ are the thermal resistances of the left and right contacts, respectively; and h is the heat transfer coefficient from the nanowire to air. Fitting the heating profile $\Delta T(x)$ along the wire gives thermal conductivity as well as the thermal contact resistances, provided there is accurate determination of P and h. In the case of Raman thermography, which employs the excitation laser as the heat source, $P = IQ_a$ where I is the total applied laser power and Q_a is the size-, refractive index-, polarization-, and wavelength-dependent absorption efficiency,[41] which we calculated using finite-difference time domain (FDTD) simulations in order to take the nanowires' specific cross-sectional shapes and the laser spot size and profile into account. We determined h for the wires studied here to be 1.8 W cm^{-2} K^{-1} by performing Raman thermography on nominally identical nanowires harvested from the same synthesis batch in both bridged and cantilevered geometries and assuming that κ, h, and R_c should be geometry independent. Losses due to radiation are negligible compared to solid or gas conduction. The model, absorption calculations, and determination of the heat transfer coefficient are discussed in detail in the Supporting Information.

We use our Raman-based scheme in situ with a MEMS-based tensile testing device capable of applying controlled nm-level displacements and measuring nN-level forces[42,43] (see Supporting Information). An optical image of the device is shown in Figure 1a, and a schematic of the device placed under the

objective of a confocal micro-Raman system is shown in Figure 1b. A representative scanning electron microscope (SEM) image of an individual nanowire clamped to the device is given in Figure 1c. Maps of spectra (Figure 1d) were obtained for nanowires subject to a uniform strain (applied using the device shown in Figure 1a) as well as for nanowires damaged via ion bombardment. Sample first-order spectra collected with low and high laser powers with and without applied uniform strain are given in Figure 1e. These peaks correspond to the strain- and temperature-dependent zone-center longitudinal optical (LO) phonon in Si. The frequencies of these spectral peaks (the Raman shifts) were determined as a function of laser position along the nanowire for each increment of power, as in Figure 2a. The lowest Raman shift occurs in the center of the nanowire, indicating the highest induced temperature; the Raman shift increases (temperature decreases) toward the grips, which serve as efficient heat sinks. We obtained additional profiles by examining the profiles laterally shifted from the nanowire axis and correcting the incident laser intensity based on the relative Raman peak intensity (see Supporting Information).

Increasing either strain, defect density, or temperature produces downshifts in the Raman peak position, and the separate contributions were decoupled by varying the laser intensity as follows. Fits of the Raman shift minima (i.e., highest temperatures) of the heating profile as a function of the total incident laser intensity for an unstrained nanowire as well as at three applied stresses are shown in Figure 2b with the slope of these fits proportional to the total thermal resistance of the system as per eq 1. The zero-intensity intercepts of the fits

shown in Figure 2b were taken to be the room-temperature peak positions for each stress increment. The differences between the unstrained and strained room-temperature peak positions are due to strain, while the difference between the room temperature peak at a given stress and the measured peaks is entirely due to laser heating. With our independent measure of stress, this decoupling procedure enabled the measurement the room-temperature relation between Raman shift and tensile stress in Si (see Supporting Information). The peak shift for a given stress was observed to be linear with laser intensity, suggesting a constant thermal resistance over the temperature range of the measurement ($\Delta T < 80$ K) and negligible resistive heating due to photocurrents, which would heat the wire as ΔP^2. The temperature (secondary axis of Figure 2a) was subsequently calculated from the spectrum as $\Delta T = (\omega - \omega_{RT})/\chi_T$, where ω is the measured peak position and ω_{RT} is the room-temperature peak position. We confirmed that the Raman shift with temperature, χ_T, is independent of strain by performing lattice dynamics simulations to extract the temperature dependence of the frequency of the zone-center optical phonon (corresponding to the first order Raman peak) at various tensile stresses. These results show χ_T to be unchanged as compared to the unstressed case (see Supporting Information).

Our results for thermal conductivity of unstrained nanowires are in excellent agreement with other groups' reports for specimens with atomic-scale roughness, demonstrating the validity of our method. The thermal conductivity values we obtained for four unstrained $\langle 111 \rangle$-oriented Si nanowires with diameters between 171 and 177 nm were between 58 and 66 W m^{-1} K^{-1} with contact resistances on the order of 1 K μW^{-1}. With our experimental setup and sample dimensions, neglecting contact resistance would yield errors of 20–25%. The first experimental measurement of thermal conductivity performed on Si nanowires used microfabricated resistive heater-thermometers on bridged nanowires[44] and this diameter-dependent data was fit to a model based on diffuse boundary scattering.[45] Predictions from this model for a circular cross-section nanowire with the diameter and roughness of the nanowires used in the present study give a thermal conductivity of approximately 60 W m^{-1} K^{-1}, which is in excellent agreement with our measurements. Our results are also in agreement with the fit to diameter-dependent measurements obtained using Raman thermography of cantilevered Si nanowires[31] from which we would predict nanowires of similar diameter to have thermal conductivity of 55 W m^{-1} K^{-1}.

We applied uniform tensile strain to wire 1 (diameter $d = 177$ nm) and measured thermal conductivity as a function of stress as shown in Figure 3. We found heat transport changes to be small, if present, for tensile stresses as high as 1.7 GPa (equivalent to an elastic strain of ~0.9%). We confirmed our results by examining the total thermal resistance calculated using eq 1, a measure independent of the resistance calculated using eq 2, and corrected for thermal contact resistance and air conduction using a lumped thermal circuit model which provides an approximate solution to the heat equation (see Supporting Information). Thermal conductivity calculated using this analysis method was in excellent agreement with the results of the exact method, as can be seen in Figure 3. Our results are furthermore consistent with recent MD simulations on Si nanowires[14] in which the effect of strain on phonon frequencies and subsequent changes in phonon velocity and
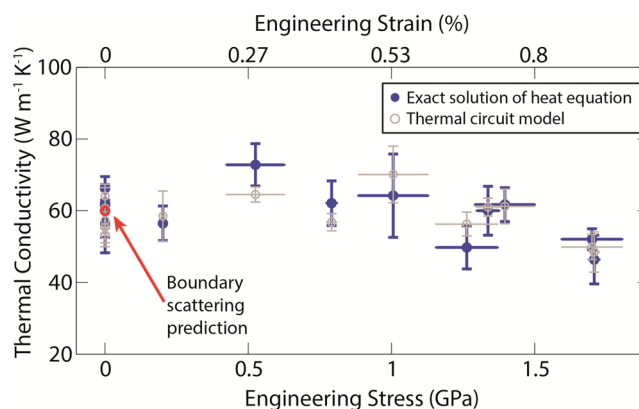

Figure 3. Thermal conductivity of an undoped, $\langle 111 \rangle$-oriented Si nanowire as a function of applied engineering stress. Details regarding the two analysis methods are given in the text. No systematic change beyond the error bars is observed. The plotted boundary scattering model point is for comparison to the model described in ref 45, which predicts a nanowire of this diameter to have thermal conductivity 60 W m^{-1} K^{-1}. Engineering strain values were calculated using the Young's modulus measured from nominally identical nanowires, which demonstrated fully elastic behavior with no permanent strains for the strain ranges used here (see Supporting Information and ref 42).

heat capacity were examined. The authors found that less than 1% strain applied to a 4 nm diameter nanowire would yield less than 1% reduction in thermal conductivity. Indeed, more than 7% strain was needed to achieve a 10% reduction, beyond the reported elastic limit of Si nanowires with these sizes.[28] We may also compare our results to experiments on undoped bulk Si under hydrostatic compressive strain up to 1 GPa,[46] which found a similarly small change in thermal conductivity. Taken as a whole, our results suggest that uniform, uniaxial elastic strains below 1% do not substantially affect phononic transport in Si nanowires.

The strain resulting from uniaxial tension is spatially uniform and thus affects phonon behavior primarily through changes to frequencies and hence heat capacity and group velocity. A contrasting view is that of strain incurred by point defects such as vacancies, which reduce the phonon mean free path due to local strain gradients, mass-difference with the host lattice, and changes to interatomic potential.[19,23,47,48] One way to introduce a large density of defects is by way of displacement damage resulting from ion irradiation. We lightly irradiated a 5 μm section in the center of wire 1 and a 4 μm section of a similarly sized wire (wire 2, $d = 175$ nm) with a focused Ga$^+$ ion beam (30 kV and fluence 4 ions nm^{-2}, see Supporting Information for more details). Figure 4a shows a dark-field transmission electron microscopy (TEM) image of wire 2 at the boundary between the irradiated and unirradiated regions with a selected area electron diffraction (SAED) pattern from the irradiated region inset. We observe a thin semishell (<25 nm) of partially amorphized Si in the irradiated region, but the majority of the wire remains crystalline (although defected as evidenced by the SAED pattern which exhibits strong spots and very faint rings). There was no overall change in diameter or surface roughness. Wires 1 and 2 exhibited drops in thermal conductivity of approximately 92% and 94%, respectively, as a result of irradiation. Figure 4b demonstrates this pronounced effect via the marked change in the relationship between laser power and peak position (slope proportional to thermal resistance) for wire 2 before and after irradiation. To verify that
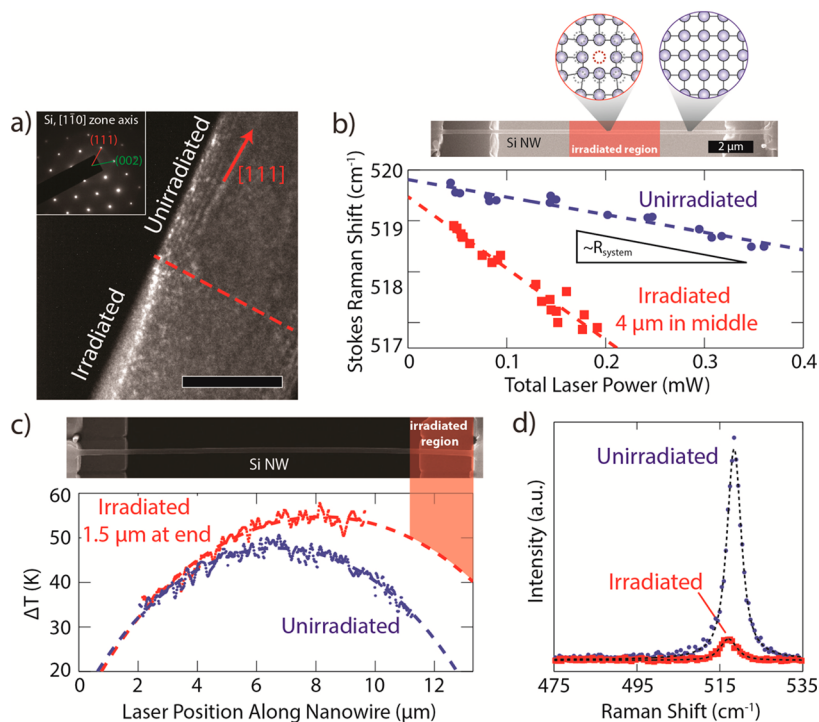
Figure 4. Point defect mediated thermal transport in ion-irradiated Si nanowires. (a) Dark-field TEM image of the irradiated/unirradiated boundary of wire 2 using the (111) spot indicated in SAED pattern from the irradiated region, inset. Scale bar represents 100 nm. (b) Raman shift as a function of incident laser intensity for wire 2 before (blue circles) and after (red squares) ion irradiation. The slope of this curve is proportional to the thermal resistance of the system. Measurements before and after irradiation were performed on the same day and within the same session in order to eliminate errors due to instrumental drift. (c) Heating profiles for fixed laser intensity for wire 3 before and after irradiating one end near a grip. (d) Direct comparison of representative Raman spectra from unirradiated and irradiated regions of wire 2 collected using the same laser intensity and collection time. Any amorphous peaks are undetectable.

the apparent heating increases in the irradiated wires were due to changes in thermal conductivity and not to changes in absorption or in χ_T in the irradiated region, a third wire (wire 3, d = 171 nm) was irradiated along a 1.5 μm length at the end of the nanowire such that all Raman measurements were performed on the pristine section of the nanowire. Changes in the heating profile for fixed laser intensity (Figure 4c) could then be attributed to changes in the resistance of the irradiated length of the nanowire. Here, a drop of 71% in thermal conductivity was observed for the irradiated section. The difference between the thermal conductivities measured using the two irradiation geometries could be due to small changes in absorption or χ_T in the irradiated region or due to changes in contact resistance upon irradiation that we were unable measure in this experimental geometry. Regardless, it is clear that the bulk of the apparent drop is due to a change in thermal conductivity within the irradiated region.

We ascribe our decrease in thermal conductivity to the introduction of defects in the form of vacancies, self-interstitials, and implanted ions[49] throughout the nanowire volume. Stopping and range of ions in matter (SRIM)[50] calculations imply that we should expect orders of magnitude more displaced Si atoms than implanted Ga^+ ions, so we expect that vacancies are the dominant defects in the irradiated nanowires. Accordingly, our Raman spectra from the irradiated regions suggest more extensive disruption of the lattice than can be seen with TEM. Compared to the perfectly crystalline case, the first-order Raman peak for Si which has been disordered via either ion implantation[51] or deposition conditions,[52] has been observed to be of lower Raman shift, lower intensity, and

broader line width. As can be seen in Figure 4b, the room-temperature peak position in the irradiated region is 0.3 cm^{-1} lower than in the unirradiated region. Furthermore, the intensity of the irradiated peak is lower by a factor of approximately 10 with no amorphous peak, as shown in representative Raman spectra collected from wire 2 in the irradiated and unirradiated regions within the same map (Figure 4d). Although more difficult to measure compared to the changes in intensity or position, we detect some (6−14%) broadening in the irradiated regions beyond what would be expected with increasing temperature. The lowered shifts and intensities and increased line widths we observe suggest phonon confinement with characteristic length scales smaller than the nanowire diameter, akin to systems with large fractions of planar defects (e.g., grain boundaries) such as nanocrystalline systems.[53,54] This interpretation is consistent with our TEM and SAED results, which indicate that the vast majority of the irradiated material maintains crystallinity, albeit with local disorder introduced via irradiation-induced defects, leading to the large measured drop in thermal conductivity. We may exclude diameter and surface effects as causes of the dramatic lowering of thermal conductivity since we observe no changes to the nanowire outer surface. Additionally, the <25 nm diameter reduction of the crystalline core is not sufficient to yield the observed >70% drops. By comparison with diameter-dependent studies, we should expect a decrease of approximately 12%,[31,45] which is an upper bound because any contribution from thermal conduction within the thin amorphous layer would be small and would only serve to increase the measured thermal conductivity. The rms roughness

of the crystalline—amorphous interface was at most 1 nm greater than the surface roughness of the unirradiated wire, also insufficient to yield the observed drops by comparison with systematic studies of roughness dependence.[55,56] A decrease in thermal conductivity with irradiation is additionally consistent with experimental reports on irradiated samples of bulk SiC[25,26] and microscale InN,[27] for which the surface and diameter effects prevalent at the nanoscale are negligible.

Our measurements suggest that the diminished thermal conductivity observed in studies of rough Si nanowires may in fact be due in large part to core rather than surface effects. Reports on the effect of surface roughness have all used metal-assisted chemical etching,[8,45,55−57] a process known to, depending on the concentrations of the etchant components, lead to the formation of nanoporous nanowires.[58,59] It has not been unequivocally demonstrated that the etched nanowires used in these surface roughening studies did not also contain an increased concentration of atomic-scale pores and vacancies (which would not be observable in conventional TEM) as compared to pristine wires. Indeed, Raman spectra of etched Si nanowires with roughness controlled by the etch time have been reported to exhibit broadening of the first-order peak that increased with etch time with lowered thermal conductivity always accompanied by significant broadening, indicating that increasing lattice disorder may have been responsible for the decrease in thermal conductivity.[56] This notion is consistent with recent MD simulations that examined Si nanowires with both surface roughness and core defects and found that a combination of the two is necessary to achieve the thermal conductivity decreases reported in the literature with core defects responsible for the majority of the reduction.[60] Our measurement of a large drop in thermal conductivity without a significant increase in surface roughness and with a broadened peak width is consistent with this notion, and it is clear that roughening approaches that do not modify the core must be developed and utilized to isolate the effect of surface quality on thermal conductivity.

Taken as a whole, our measurements imply that point defects radically affect thermal transport in Si, whereas small, uniform elastic strains do so weakly. The decrease in Si thermal conductivity with uniform tensile strain arises from a reduction of phonon frequencies and hence heat capacity and phonon velocity.[14] For the elastic strains achieved here (<0.9%), the change in zone-center phonon frequency is relatively small (<1.1%, as seen from our room-temperature Raman shifts) and the effect on thermal conductivity is also relatively small. This implies that uniaxial strain may be used to independently tune electrical properties without strongly influencing thermal transport, a promising indicator of the use of elastic strain engineering in applications benefiting from tunable charge transport or optical properties. Irradiation has a more drastic effect on thermal properties by significantly decreasing phonon scattering times due to defects, primarily vacancies, due to localized changes in mass, interatomic potential, and strain. Atomistic simulations that have examined the relative weights of these mechanisms for vacancies have suggested that the strain effect dominates over the mass effect,[22,61] contrary to, for instance, scattering from substitutional impurities where the two contributions to the scattering time have been found to be of the same order.[62] This is perhaps due to differing magnitudes of strain. For the stable vacancy clusters in Si predicted from first-principles calculations, bond lengths near a vacancy are extended by up to 17%,[63] four to five times the strain that has

been measured near dopants in Si.[64] However, the simulations that attempt to distinguish the effects of the various phonon scattering mechanisms from vacancies do not address changes in interatomic potential or account for vacancy clustering and the associated changes in bond strength and angle, so it is clear that much work must still be done. Nevertheless, the role of lattice disorder owing to irradiation-induced defects in drastically reducing thermal conductivity is clear.

We expect the method presented here to be widely applicable for characterizing the thermal and phononic behavior of any Raman-active system that may be laser-heated. Determination of the room-temperature peak position makes the method particularly useful when the positions of peaks in the Raman spectrum do not exactly correspond to the bulk due to nanostructuring, alloying, doping, defects, or strain. We note that of the various mechanisms behind phonon scattering from defects, locally heterogeneous strain is believed to play a role, which is in contrast with our finding that uniform, uniaxial strain is an ineffective modifier of phonon transport. This may imply that the state of strain is far more important than the presence of strain, and reversibly introducing strain gradients may present a new direction for adaptively tuning thermal conductivity, for example, by straining a tapered or kinked nanowire or by buckling. Two-dimensional systems that, like one-dimensional systems, may accommodate more strain than their bulk counterparts, present further opportunities for producing reversible strain gradients, for example, by indenting graphene or dichalcogenides or by applying tensile strain to micro- or nanoporous thin films. We additionally note that our measurements probe the total thermal conductivity (κ_{total}), which includes contributions from both charge carriers (κ_{el}) and the lattice (κ_{ph}). Room temperature, undoped Si has κ_{el} on the order of 1 nW m^{-1} K^{-1}, whereas κ_{total} = 150 W m^{-1} K^{-1},[65] but systems with very low thermal conductivity and highly strain-sensitive electrical conductivity may exhibit a more significant effect. For instance, the study of SiGe nanowires, which have thermal conductivity nearly an order of magnitude lower than single-crystal Si nanowires of the same size[66] and piezoresistive gauge factors several times that of Si,[67] could be another interesting avenue of research.

Conclusions. We have measured the effect of both uniform tensile strain and point defects on thermal conductivity in a single nanostructure using Raman piezothermography. Up to 1.7 GPa of unixial tensile stress was applied to a ⟨111⟩ Si nanowire, and spatially resolved maps of Raman spectra at several laser powers were used to decouple the effects of strain and temperature in order to calculate thermal conductivity. No change in thermal conductivity was observed for these uniaxially strained nanowires but when defects were introduced via Ga$^+$ irradiation, near-order-of-magnitude decreases in thermal conductivity were realized due to enhanced phonon scattering. Our results also show that thermal conductivity decreases in nanowires previously attributed to surface roughness may in fact be due to core defects created during the fabrication of roughened nanowires. It follows that point defects and potentially the large strain gradients surrounding such defects have a far larger effect on thermal conductivity than surface roughness or unixial strain do, pointing toward new means of controlling and tuning thermal transport.

■ ASSOCIATED CONTENT

Ⓢ Supporting Information

Nanowire characterization, MEMS-based tensile testing, Raman mapping, exact and approximate heating profiles for bridged and cantilevered nanowires, absorption calculations, heat losses to air conduction and radiation, Raman-based stress measurement, MD simulations to determine χ_T as a function of stress, correction for nanowire heating from the thermal actuator, details of ion irradiation, and error estimates. This material is available free of charge via the Internet at http://pubs.acs.org.

■ AUTHOR INFORMATION

Corresponding Author

*E-mail: Gianola@seas.upenn.edu.

Author Contributions

The manuscript was written through contributions of all authors. All authors have given approval to the final version of the manuscript.

Notes

The authors declare no competing financial interest.

■ ACKNOWLEDGMENTS

■ REFERENCES

(1) Snyder, G. J.; Toberer, E. S. Complex Thermoelectric Materials. *Nat. Mater.* **2008**, *7*, 105−114.

(2) Zebarjadi, M.; Esfarjani, K.; Dresselhaus, M. S.; Ren, Z. F.; Chen, G. Perspectives on Thermoelectrics: From Fundamentals to Device Applications. *Energy Environ. Sci.* **2012**, *5*, 5147−5162.

(3) Sun, Y.; Rogers, J. A. Inorganic Semiconductors for Flexible Electronics. *Adv. Mater.* **2007**, *19*, 1897−1916.

(4) Kraemer, D.; Poudel, B.; Feng, H.-P.; Caylor, J. C.; Yu, B.; Yan, X.; Ma, Y.; Wang, X.; Wang, D.; Muto, A.; et al. High-Performance Flat-Panel Solar Thermoelectric Generators with High Thermal Concentration. *Nat. Mater.* **2011**, *10*, 532−538.

(5) Licht, S.; Wang, B.; Ghosh, S.; Ayub, H.; Jiang, D.; Ganley, J. A New Solar Carbon Capture Process: Solar Thermal Electrochemical Photo (STEP) Carbon Capture. *J. Phys. Chem. Lett.* **2010**, *1*, 2363−2368.

(6) Maldovan, M. Sound and Heat Revolutions in Phononics. *Nature* **2013**, *503*, 209−217.

(7) Boukai, A. I.; Bunimovich, Y.; Tahir-Kheli, J.; Yu, J.-K.; Goddard, W. A., III; Heath, J. R. Silicon Nanowires as Efficient Thermoelectric Materials. *Nature* **2008**, *451*, 168−171.

(8) Hochbaum, A. I.; Chen, R.; Delgado, R. D.; Liang, W.; Garnett, E. C.; Najarian, M.; Majumdar, A.; Yang, P. Enhanced Thermoelectric Performance of Rough Silicon Nanowires. *Nature* **2008**, *451*, 163−167.

(9) Li, B.; Wang, L.; Casati, G. Negative Differential Thermal Resistance and Thermal Transistor. *Appl. Phys. Lett.* **2006**, *88*, 143501.

(10) Chu, M.; Sun, Y.; Aghoram, U.; Thompson, S. E. Strain: A Solution for Higher Carrier Mobility in Nanoscale MOSFETs. *Annu. Rev. Mater. Res.* **2009**, *39*, 203−229.

(11) Picu, R. C.; Borca-Tasciuc, T.; Pavel, M. C. Strain and Size Effects on Heat Transport in Nanostructures. *J. Appl. Phys.* **2003**, *93*, 3535−3539.

(12) Bhowmick, S.; Shenoy, V. B. Effect of Strain on the Thermal Conductivity of Solids. *J. Chem. Phys.* **2006**, *125*, 164513.

(13) Zhu, L.; Zheng, X. Modification of the Phonon Thermal Conductivity in Spatially Confined Semiconductor Nanofilms under Stress Fields. *Europhys. Lett.* **2009**, *88*, 36003.

(14) Li, X.; Maute, K.; Dunn, M.; Yang, R. Strain Effects on the Thermal Conductivity of Nanostructures. *Phys. Rev. B* **2010**, *81*, 245318.

(15) Abramson, A. R.; Tien, C.-L.; Majumdar, A. Interface and Strain Effects on the Thermal Conductivity of Heterostructures: A Molecular Dynamics Study. *J. Heat Transfer* **2002**, *124*, 963−970.

(16) Lee, S.-M.; Cahill, D. G.; Venkatasubramanian, R. Thermal Conductivity of Si−Ge Superlattices. *Appl. Phys. Lett.* **1997**, *70*, 2957−2959.

(17) Cahill, D. G.; Ford, W. K.; Goodson, K. E.; Mahan, G. D.; Majumdar, A.; Maris, H. J.; Merlin, R.; Phillpot, S. R. Nanoscale Thermal Transport. *J. Appl. Phys.* **2003**, *93*, 793−818.

(18) Huxtable, S. T.; Abramson, A. R.; Tien, C.-L.; Majumdar, A.; LaBounty, C.; Fan, X.; Zeng, G.; Bowers, J. E.; Shakouri, A.; Croke, E. T. Thermal Conductivity of Si/SiGe and SiGe/SiGe Superlattices. *Appl. Phys. Lett.* **2002**, *80*, 1737−1739.

(19) Klemens, P. G. The Scattering of Low-Frequency Lattice Waves by Static Imperfections. *Proc. Phys. Soc. A* **1955**, *68*, 1113−1128.

(20) Zou, J.; Kotchetkov, D.; Balandin, A. A.; Florescu, D. I.; Pollak, F. H. Thermal Conductivity of GaN Films: Effects of Impurities and Dislocations. *J. Appl. Phys.* **2002**, *92*, 2534−2539.

(21) Lee, Y.; Lee, S.; Hwang, G. Effects of Vacancy Defects on Thermal Conductivity in Crystalline Silicon: A Nonequilibrium Molecular Dynamics Study. *Phys. Rev. B* **2011**, *83*, 125202.

(22) Zhang, X.; Sun, Z. Effects of Vacancy Structural Defects on the Thermal Conductivity of Silicon Thin Films. *J. Semicond.* **2011**, *32*, 053002.

(23) Carruthers, P. Scattering of Phonons by Elastic Strain Fields and the Thermal Resistance of Dislocations. *Phys. Rev.* **1959**, *114*, 995−1001.

(24) Dhara, S.; Solanki, H. S.; Pawan, R. A.; Singh, V.; Sengupta, S.; Chalke, B. A.; Dhar, A.; Gokhale, M.; Bhattacharya, A.; Deshmukh, M. M.; et al. Tunable Thermal Conductivity in Defect Engineered Nanowires at Low Temperatures. *Phys. Rev. B* **2011**, *84*, 121307.

(25) Rohde, M. Reduction of the Thermal Conductivity of SiC by Radiation Damage. *J. Nucl. Mater.* **1991**, *182*, 87−92.

(26) Price, R. J. Thermal Conductivity of Neutron-Irradiated Pyrolytic Beta-Silicon Carbide. *J. Nucl. Mater.* **1973**, *46*, 268−272.

(27) Levander, A. X.; Tong, T.; Yu, K. M.; Suh, J.; Fu, D.; Zhang, R.; Lu, H.; Schaff, W. J.; Dubon, O.; Walukiewicz, W.; et al. Effects of Point Defects on Thermal and Thermoelectric Properties of InN. *Appl. Phys. Lett.* **2011**, *98*, 012108.

(28) Zhu, Y.; Xu, F.; Qin, Q.; Fung, W. Y.; Lu, W. Mechanical Properties of Vapor-Liquid-Solid Synthesized Silicon Nanowires. *Nano Lett.* **2009**, *9*, 3934−3939.

(29) Minamisawa, R. A.; Süess, M. J.; Spolenak, R.; Faist, J.; David, C.; Gobrecht, J.; Bourdelle, K. K.; Sigg, H. Top-down Fabricated Silicon Nanowires under Tensile Elastic Strain up to 4.5%. *Nat. Commun.* **2012**, *3*, 1096.

(30) Balandin, A. A.; Ghosh, S.; Bao, W.; Calizo, I.; Teweldebrhan, D.; Miao, F.; Lau, C. N. Superior Thermal Conductivity of Single-Layer Graphene. *Nano Lett.* **2008**, *8*, 902−907.

(31) Doerk, G. S.; Carraro, C.; Maboudian, R. Single Nanowire Thermal Conductivity Measurements by Raman Thermography. *ACS Nano* **2010**, *4*, 4908−4914.

(32) Soini, M.; Zardo, I.; Uccelli, E.; Funk, S.; Koblmüller, G.; Fontcuberta i Morral, A.; Abstreiter, G. Thermal Conductivity of GaAs Nanowires Studied by Micro-Raman Spectroscopy Combined with Laser Heating. *Appl. Phys. Lett.* **2010**, *97*, 263107.

(33) Li, Q.; Liu, C.; Wang, X.; Fan, S. Measuring the Thermal Conductivity of Individual Carbon Nanotubes by the Raman Shift Method. *Nanotechnology* **2009**, *20*, 145702.

(34) Hsu, I.-K.; Pettes, M. T.; Bushmaker, A.; Aykol, M.; Shi, L.; Cronin, S. B. Optical Absorption and Thermal Transport of Individual Suspended Carbon Nanotube Bundles. *Nano Lett.* **2009**, *9*, 590−594.

(35) Ghosh, S.; Calizo, I.; Teweldebrhan, D.; Pokatilov, E. P.; Nika, D. L.; Balandin, A. A.; Bao, W.; Miao, F.; Lau, C. N. Extremely High Thermal Conductivity of Graphene: Prospects for Thermal Management Applications in Nanoelectronic Circuits. *Appl. Phys. Lett.* **2008**, *92*, 151911.

(36) Cai, W.; Moore, A. L.; Zhu, Y.; Li, X.; Chen, S.; Shi, L.; Ruoff, R. S. Thermal Transport in Suspended and Supported Monolayer Graphene Grown by Chemical Vapor Deposition. *Nano Lett.* **2010**, *10*, 1645−1651.

(37) Balandin, A. A. Thermal Properties of Graphene and Nanostructured Carbon Materials. *Nat. Mater.* **2011**, *10*, 569−581.

(38) Yan, R.; Simpson, J. R.; Bertolazzi, S.; Brivio, J.; Watson, M.; Wu, X.; Kis, A.; Luo, T.; Hight Walker, A. R.; Xing, H. G. Thermal Conductivity of Monolayer Molybdenum Disulfide Obtained from Temperature-Dependent Raman Spectroscopy. *ACS Nano* **2014**, *8*, 986−993.

(39) Ghosh, S.; Nika, D. L.; Pokatilov, E. P.; Balandin, A. A. Heat Conduction in Graphene: Experimental Study and Theoretical Interpretation. *New J. Phys.* **2009**, *11*, 095012.

(40) Doerk, G. S.; Carraro, C.; Maboudian, R. Temperature Dependence of Raman Spectra for Individual Silicon Nanowires. *Phys. Rev. B* **2009**, *80*, 073306.

(41) Cao, L.; White, J. S.; Park, J.-S.; Schuller, J. A.; Clemens, B. M.; Brongersma, M. L. Engineering Light Absorption in Semiconductor Nanowire Devices. *Nat. Mater.* **2009**, *8*, 643−647.

(42) Murphy, K. F.; Chen, L. Y.; Gianola, D. S. Effect of Organometallic Clamp Properties on the Apparent Diversity of Tensile Response of Nanowires. *Nanotechnology* **2013**, *24*, 235704.

(43) Chen, L. Y.; Richter, G.; Sullivan, J. P.; Gianola, D. S. Lattice Anharmonicity in Defect-Free Pd Nanowhiskers. *Phys. Rev. Lett.* **2012**, *109*, 125503.

(44) Li, D.; Wu, Y.; Kim, P.; Shi, L.; Yang, P.; Majumdar, A. Thermal Conductivity of Individual Silicon Nanowires. *Appl. Phys. Lett.* **2003**, *83*, 2934−2936.

(45) Chen, R.; Hochbaum, A. I.; Murphy, P.; Moore, J.; Yang, P.; Majumdar, A. Thermal Conductance of Thin Silicon Nanowires. *Phys. Rev. Lett.* **2008**, *101*, 105501.

(46) Andersson, S.; Backstrom, G. The Thermal Conductivity and Heat Capacity of Single-Crystal Si under Hydrostatic Pressure. *J. Phys. C: Solid State Phys.* **1988**, *21*, 3727−3735.

(47) Slack, G. A. Effect of Isotopes on Low-Temperature Thermal Conductivity. *Phys. Rev.* **1957**, *105*, 829−831.

(48) Gibbons, T. M.; Kang, B.; Estreicher, S. K.; Carbogno, C. Thermal Conductivity of Si Nanostructures Containing Defects: Methodology, Isotope Effects, and Phonon Trapping. *Phys. Rev. B* **2011**, *84*, 035317.

(49) Rubanov, S.; Munroe, P. R. FIB-Induced Damage in Silicon. *J. Microsc.* **2004**, *214*, 213−221.

(50) Ziegler, J. F.; Biersack, J. P.; Ziegler, M. D. *SRIM, The Stopping and Range of Ions in Matter*; Lulu Press Co.: 860 Aviation Parkway; Suite 300; Morrisville, North Carolina 27560, United States, 2008.

(51) Villeneuve, C.; Bourdelle, K. K.; Paillard, V.; Hebras, X.; Kennard, M. Raman Spectroscopy Study of Damage and Strain in (001) and (011) Si Induced by Hydrogen or Helium Implantation. *J. Appl. Phys.* **2007**, *102*, 094905.

(52) Tay, L.; Lockwood, D. J.; Baribeau, J.-M.; Wu, X.; Sproule, G. I. Raman and Transmission Electron Microscopy Study of Disordered Silicon Grown by Molecular Beam Epitaxy. *J. Vac. Sci. Technol., A* **2004**, *22*, 943−947.

(53) Campbell, I. H.; Fauchet, P. M. The Effects of Microcrystal Size and Shape on the One Phonon Raman Spectra of Crystalline Semiconductors. *Solid State Commun.* **1986**, *58*, 739−741.

(54) Richter, H.; Wang, Z. P.; Ley, L. The One Phonon Raman Spectrum in Microcrystalline Silicon. *Solid State Commun.* **1981**, *39*, 625−629.

(55) Lim, J.; Hippalgaonkar, K.; Andrews, S. C.; Majumdar, A.; Yang, P. Quantifying Surface Roughness Effects on Phonon Transport in Silicon Nanowires. *Nano Lett.* **2012**, *12*, 2475−2482.

(56) Feser, J. P.; Sadhu, J. S.; Azeredo, B. P.; Hsu, K. H.; Ma, J.; Kim, J.; Seong, M.; Fang, N. X.; Li, X.; Ferreira, P. M.; et al. Thermal Conductivity of Silicon Nanowire Arrays with Controlled Roughness. *J. Appl. Phys.* **2012**, *112*, 114306.

(57) Ghossoub, M. G.; Valavala, K. V.; Seong, M.; Azeredo, B.; Hsu, K.; Sadhu, J. S.; Singh, P. K.; Sinha, S. Spectral Phonon Scattering from Sub-10 Nm Surface Roughness Wavelengths in Metal-Assisted Chemically Etched Si Nanowires. *Nano Lett.* **2013**, *13*, 1564−1571.

(58) Lee, D. H.; Kim, Y.; Doerk, G. S.; Laboriante, I.; Maboudian, R. Strategies for Controlling Si Nanowire Formation during Au-Assisted Electroless Etching. *J. Mater. Chem.* **2011**, *21*, 10359.

(59) Huang, Z.; Geyer, N.; Werner, P.; de Boor, J.; Gösele, U. Metal-Assisted Chemical Etching of Silicon: A Review. *Adv. Mater.* **2011**, *23*, 285−308.

(60) He, Y.; Galli, G. Microscopic Origin of the Reduced Thermal Conductivity of Silicon Nanowires. *Phys. Rev. Lett.* **2012**, *108*, 215901.

(61) Chen, Y.; Lukes, J. R.; Li, D.; Yang, J.; Wu, Y. Thermal Expansion and Impurity Effects on Lattice Thermal Conductivity of Solid Argon. *J. Chem. Phys.* **2004**, *120*, 3841−3846.

(62) Asheghi, M.; Kurabayashi, K.; Kasnavi, R.; Goodson, K. E. Thermal Conduction in Doped Single-Crystal Silicon Films. *J. Appl. Phys.* **2002**, *91*, 5079.

(63) Lee, S.; Hwang, G. Theoretical Determination of Stable Fourfold Coordinated Vacancy Clusters in Silicon. *Phys. Rev. B* **2008**, *78*, 125310.

(64) Wei, S.; Oyanagi, H.; Kawanami, H.; Sakamoto, K.; Sakamoto, T.; Tamura, K.; Saini, N. L.; Uosaki, K. Local Structures of Isovalent and Heterovalent Dilute Impurities in Si Crystal Probed by Fluorescence X-Ray Absorption Fine Structure. *J. Appl. Phys.* **1997**, *82*, 4810.

(65) Glassbrenner, C. J.; Slack, G. A. Thermal Conductivity of Silicon and Germanium from 3K to the Melting Point. *Phys. Rev.* **1964**, *134*, A1058−A1069.

(66) Yin, L.; Kyung Lee, E.; Woon Lee, J.; Whang, D.; Lyong Choi, B.; Yu, C. The Influence of Phonon Scatterings on the Thermal Conductivity of SiGe Nanowires. *Appl. Phys. Lett.* **2012**, *101*, 043114.

(67) Murphy-Armando, F.; Fahy, S. Giant Piezoresistance in Silicon-Germanium Alloys. *Phys. Rev. B* **2012**, *86*, 035205.

Supporting Information:

Strain- and Defect-Mediated Thermal Conductivity in Silicon Nanowires

Kathryn F. Murphy[1], Brian Piccione[1], Mehdi B. Zanjani[2], Jennifer R. Lukes[2], Daniel S. Gianola[1*]

[1]Department of Materials Science and Engineering, University of Pennsylvania, Philadelphia, PA, USA

[2]Department of Mechanical Engineering and Applied Mechanics, University of Pennsylvania, Philadelphia, PA, USA

*Email: Gianola@seas.upenn.edu

Contents:

1. Nanowire characterization

Vapor-liquid-solid-grown, <111>-oriented Si nanowires of a narrow range of diameters (d=170 to 180 nm) were purchased from Sigma Aldrich. Several nominally identical Si nanowires (Δd<10 nm) to those used for the thermal conductivity measurements discussed here have been mechanically tested under uniaxial tension, the results of which have been discussed elsewhere.[1] Stress-strain curves are linear (see Figure S1a) and recover the bulk Young's modulus for the range of stresses used here, indicating no deviation from bulk mechanical behavior or the harmonic approximation.

Following thermal testing, nanowires were cut near one end using a FIB and then bent towards the pole piece of an SEM using a nanomanipulator, enabling end-on imaging for precise measurements of cross-sectional shape, area, and circumference. Nanowires are of a rounded triangular shape, as can be seen in Figure S1b.
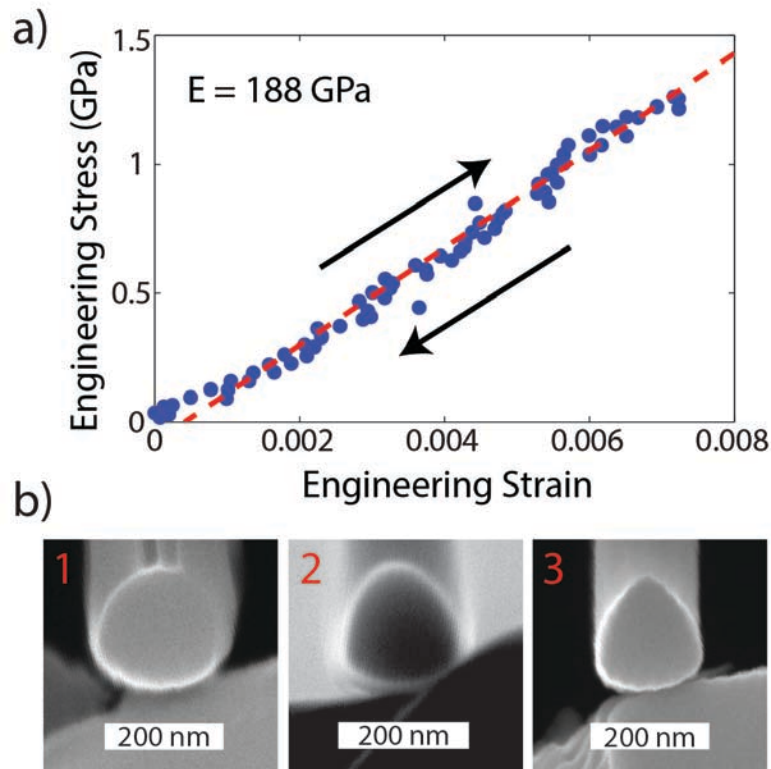

Figure S1: a) Stress-strain curve of a similarly-sized nanowire from the same batch as the nanowires used for thermal conductivity measurements. The Young's modulus is identical to that of bulk Si along the <111> direction. b) Cross-sectional image of wires 1-3.

2. MEMS-based tensile testing

The MEMS-based tensile testing device used to apply uniaxial tensile strain to individual Si nanowires consists of a suspended thermal actuator, which is electrically and thermally isolated from the grip region, and a suspended compound flexure load cell with a stiffness of 44 N m⁻¹. Since the load cell compliance was nearly an order of magnitude higher than that of the nanowire, we avoided errors due to compressive stresses from thermal expansion (see section 11). Nanowires were drop cast onto a lacey carbon TEM grid and single nanowires were harvested using a nanomanipulator inside a SEM. The nanowire was aligned to the grips of the MEMS device and clamped using electron beam induced deposition (EBID) of a platinum-containing organometallic compound, as shown in main text Figure 1c. The gauge lengths of the wires between the two grips was 12.4 to 14.5 μm. The device was actuated to produce quasi-static strain rates in the nanowires (10^{-3} s⁻¹ to 10^{-4} s⁻¹) between strain increments. A series of images were obtained during actuation with an optical camera, and the load applied was determined using digital image correlation (DIC) to yield sub-pixel displacement resolution below 10 nm. Load differences were measured both on loading and unloading in order to verify that no relaxation occurred in the nanowire or in the contacts during Raman scanning.

3. Heating profile in a doubly-clamped nanowire

The steady-state heat equation for the temperature rise $\Delta T = T - T_{ambient}$ at position s in a one-dimensional conductor of length L, cross-sectional area A, circumference C, heated from some point in the interior a distance a and L-a from the two heat sinks (see Figure S2) may be written as:[2,3]

$$\kappa \frac{d^2 \Delta T}{ds^2} - \frac{Ch}{A} \Delta T + \frac{P}{\sqrt{\pi} w A} e^{-s^2/w^2} = 0 \qquad (S1)$$

with boundary conditions

$$\Delta T(-a) = R_{c,l} A \kappa \frac{d\Delta T}{ds}\bigg|_{s=-a}$$

$$\Delta T(L-a) = -R_{c,r} A \kappa \frac{d\Delta T}{ds}\bigg|_{s=L-a}$$

where h is the heat transfer coefficient, κ is the thermal conductivity, P is the absorbed power, w is the half-width of the laser spot, and $R_{c,l}$ and $R_{c,r}$ are the thermal contact resistances at the right and left heat sinks, respectively. The laser power source is represented by a Gaussian centered at s=0. The solution gives the full temperature distribution in the nanowire, but we are only

interested in the temperature rise at the laser spot as the distance a is varied. Setting $x{=}0$ and taking the limit as w approaches 0 (a reasonable simplification since, at 290 nm, the real w is approximately 2% the length of the nanowire) we obtain equation 2 from the main text, where now the independent variable x is the distance from the laser to the left heat sink:

$$\Delta T(x) = P \frac{\left[MR_{c,r}\cosh(m(L-x)) + \sinh(m(L-x))\right]\left[MR_{c,l}\cosh(mx) + \sinh(mx)\right]}{M\left[M(R_{c,l} + R_{c,r})\cosh(mL) + (1 + M^2 R_{c,l}R_{c,r})\sinh(mL)\right]}$$

where $M \equiv \sqrt{ChA\kappa}$ and $m \equiv \sqrt{Ch/A\kappa}$.
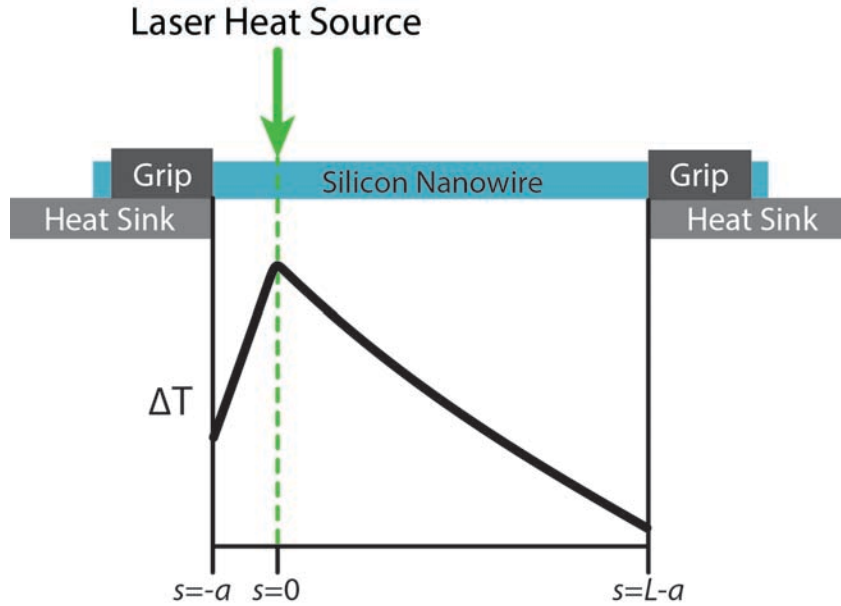
.

Figure S2: Schematic of setup for determination of the heating profile as a function of laser position. The solution to the heat equation yields temperature profiles similar to the representative profile shown. This function is solved for $s{=}0$ to obtain the rise in temperature at the laser spot. By varying a we obtain the temperature rise at the laser spot as the laser is scanned across the nanowire.

4. Raman mapping of strained and unstrained nanowires

Maps of spectra were obtained by placing the MEMS device with a clamped Si nanowire under the objective of a confocal micro-Raman system equipped with a 532 nm continuous-wave laser at ambient temperature and pressure. For the unstrained state and upon application of each increment of strain, spectra were collected along the central 9-10 μm of the nanowire length and across the nanowire diameter with a 100 nm step size. Laser intensity was precisely controlled with a neutral density filter, and at least five different powers in the range of 40 to 400 μW (as measured using a power meter at the focal point) were used. Both strain and laser power increments were varied non-monotonically to rule out systemic measurement errors and strain relaxation. Care was taken to not expose the EBID clamp material to the laser at any intensity in order to avoid heating and degradation of the clamps, as well as any potential laser-induced diffusion of the clamp material down the nanowire. The first-order Stokes peak (~520 cm^{-1} for Si at room temperature and zero strain) for each spectrum was fit to a Gaussian + Lorentzian lineshape to extract peak intensities, linewidths, and frequencies, and maps of these fits were interpolated using cubic splines. Exact nanowire position was determined from the pixels with maxima in peak intensity. Heating of the sample due to the thermal actuator was accounted and corrected for by measuring the temperature gradient in the wire at very low laser power (see section 12).

The spatially resolved maps of Raman spectra allows us to establish which spectra were obtained when the laser was centered on the nanowire by examination of the Raman peak intensity: the highest intensity spectra were acquired using the highest laser power (equivalently, when the laser was centered), as in Figure S3a. We gain additional information by examining spectra collected when the laser was off the nanowire axis, but the incident laser power must then be determined. To find the incident laser power for off-axis spectra, we calculated the ratio between the average peak intensity when the laser was centered and the average when the laser was off-axis, as can be seen in Figure S3b. We then assumed this ratio to be the same as the relative incident laser powers. The absorbed laser power when the laser was centered was determined using FDTD simulations, as discussed in this document as well as in the main text, so we can then solve for the off-axis laser intensity. The inclusion of off-axis profiles had a negligible effect on the fit to the plot of Raman shift as a function of laser power but resulted in more heating profiles (as in Figure S3c) and thus more thermal conductivity and contact resistance data points.
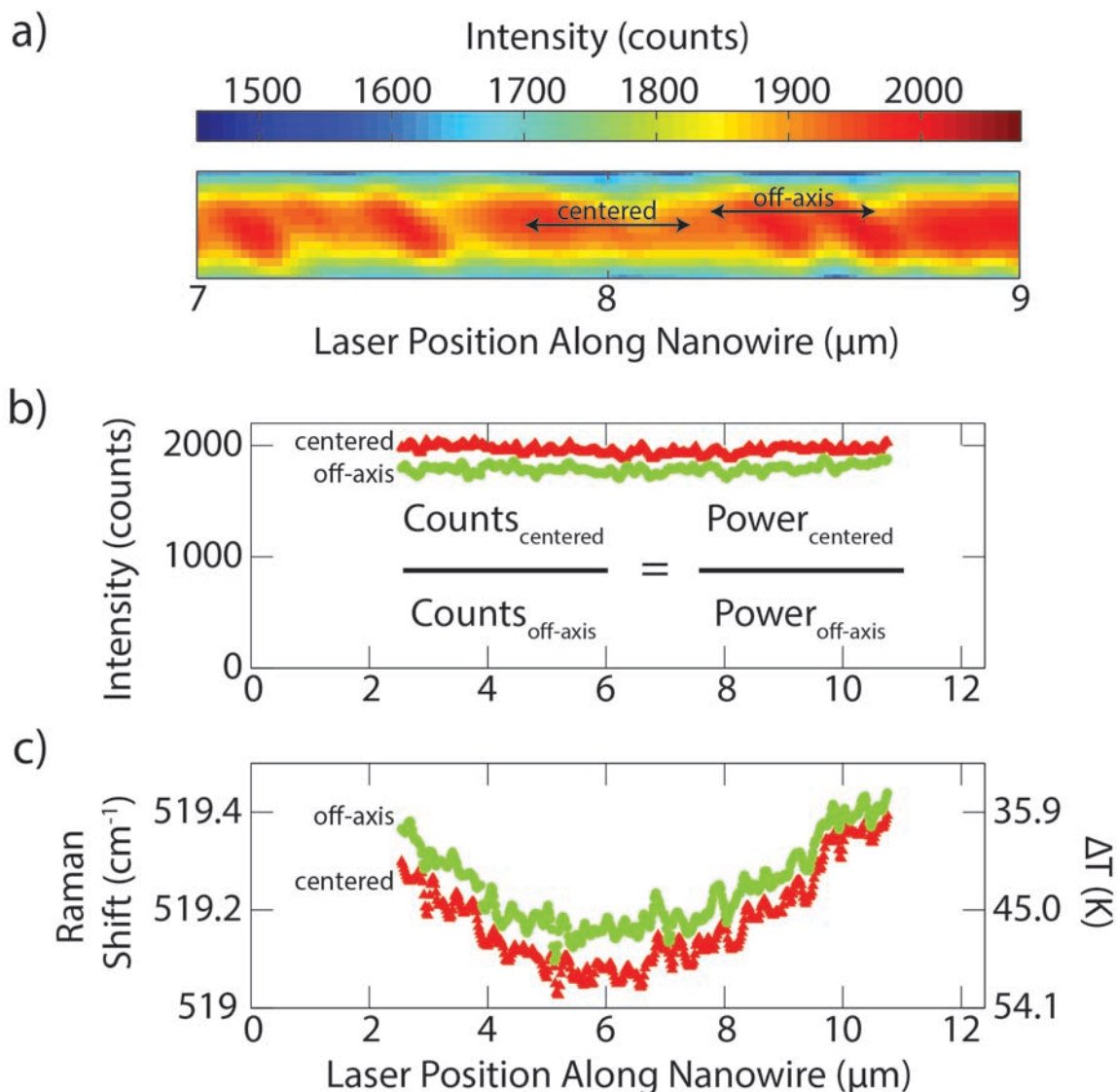
$$\frac{Counts_{centered}}{Counts_{off\text{-}axis}} = \frac{Power_{centered}}{Power_{off\text{-}axis}}$$

Figure S3: Scheme for determining power absorbed when the laser is not centered on the nanowire. a) 2 μm section of an interpolated Raman peak intensity map for unstrained wire 1. The laser was assumed to be centered on the nanowire where there were maxima in peak intensity. b) First-order Raman peak intensity for the center and laterally shifted from the nanowire axis. The absorbed power for the original data was calculated using the FDTD method described in the Supplemental Information. The absorbed power for the off-axis data was calculated from the ratio of the peak intensities (about 0.91 here) and the absorbed power for the original data. c) Corresponding Raman shift profiles for the original and off-axis data. The temperature difference is approximately 4 K.

5. Calculations of laser power absorption in non-cylindrical nanowires

Knowing exact values for the fractopm of incident power absorbed is critical to our methodology. At the nanoscale, this quantity is highly sensitive to size and shape and must be precisely determined. Absorption for silicon nanowires with a circular cross-section is known from analytical Mie scattering solutions,[4] but significant deviations from circular cross-sections in our nanowires prevent application of an analytical solution. Using a commercial finite-difference time-domain (FDTD) software package (Lumerical), 3D numerical simulations were performed for the Si nanowires with a Gaussian source focused to a FWHM of 570 nm to match measured experimental conditions. Non-circular cross-sections were obtained by fitting polynomials to cross-sectional nanowire images obtained via SEM (Figure S4a), and power absorbed per unit volume in the simulated structures was calculated from the divergence of the Poynting vector $P_{abs}=-0.5\omega|E|^2 imag(\varepsilon)$, where ω is frequency, $|E|^2$ the electric field intensity, and ε the permittivity). Integrating $|E|^2$ over the entire illuminated nanowire volume (Figure S4b) produced total power absorbed. The refractive index of Si was taken from Ref. S5. A range of frequencies about 563.5 THz with a bandwidth of 30 THz were applied to each wire to simulate the effects of scaling nanowire cross-sectional area and ensure measurement errors would not result in incorrect absorption values. No resonance peaks were found, and calculated absorption values were stable to ~0.2% within the frequency range tested. Values for wires 1-4 varied between 4.9% and 6.1%. By contrast, absorption in cylinders of the same major diameters (171-177 nm) calculated using the Mie solutions and accounting for the relative sizes of the laser spot and the nanowire is 3.1-4.4%.
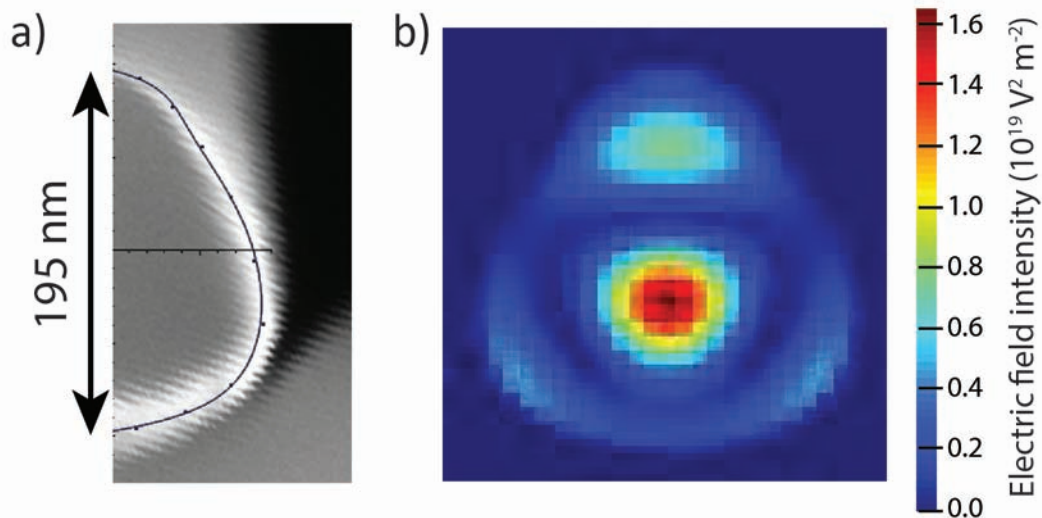

Figure S4: a) Fitted nanowire profile overlaid on cross-sectional SEM image. b) Cross-section of simulated nanowire under far-field illumination, illustrating spatial distribution of electric field intensity for 532 nm wavelength light.

6. Heat losses due to air conduction

For fixed surroundings, thermal conductivity and the heat transfer coefficient should not depend on how the sample is clamped—that is, if the wire is in bridged or cantilevered geometry, h and κ should be the same. Keeping this in mind, the thermal measurement procedure for bridged nanowires described in the main text was performed on wire 4 (d=175 nm). Following testing, the wire was cut at one end using a focused ion beam to create a cantilever and the measurement procedure was repeated. We may then modify the boundary conditions of equation S1 to allow for air conduction from the tip:[6]

$$\Delta T(-a) = R_{c,l} A \kappa \frac{d\Delta T}{dx}\bigg|_{x=-a}$$

$$\Delta T(L - a) = -\frac{\kappa}{h} \frac{d\Delta T}{dx}\bigg|_{x=L-a}$$

so we can subsitute $-\kappa/h$ for $-R_{c,r}A\kappa$ in equation 2:

$$T(s) = P\frac{\big[(M/Ah)\cosh(m(L-s))+\sinh(m(L-s))\big]\big[MR_{c,l}\cosh(ms)+\sinh(ms)\big]}{M\big[M(R_{c,l}+1/Ah)\cosh(mL)+(1+M^2 R_{c,l}/Ah)\sinh(mL)\big]} \qquad (S2)$$

We fit both the bridged and cantilevered heating profiles (see Figure S5a) using various fixed values of the heat transfer coefficient and extracted thermal conductivity from the fit. The intersection of the h vs. κ curves seen in Figure S5b represents the value of h which yields the same calculated value of κ for both clamping geometries; this intersection occurred at h=1.8 W cm^{-2} K^{-1} and κ=52 W m^{-1} K^{-1}. All measurements were performed in a sealed enclosure to minimize air currents. Figure S5c shows a heating profile fit to curves which do and do not account for heat loss to air; although both curves fit the profile well, not accounting for air losses (*i.e.*, treating h=0) leads to a 19% increase in the calculated thermal conductivity, highlighting the importance of measuring and accounting for heat losses to air. The difference would be expected to be more pronounced for thinner nanowires, which have both higher h and lower κ.

Although the value of h we measure differs from other diameter-dependent experimental measurements of h, which we would predict h to be near 0.50 W cm^{-2} K^{-1},[7] it is in good agreement with the value we calculate using a semi-empirical model from Wang *et al.*[8] based on measurements performed on microwires and carbon nanotubes. This two-layer model appropriate for quasi-1D particles with diameter approaching the mean free path of air molecules treats the transition region near the particle surface using molecular kinetics and the region farther from the particle as a continuum.[8] Within this model, the heat transfer coefficient is related to the mean free path and heat capacity of air as well as the particle diameter via the dimensionless Nusselt number, *Nu*:

$$Nu = \frac{2rh}{\kappa_{air}} = \frac{4\alpha_f f_{ncr}\zeta / \pi}{\beta + f_{ncr}(\zeta + \Delta / \lambda)\ln(n_r((\zeta + r_0 / \lambda)/(\zeta + \Delta / \lambda)))} \qquad (S3)$$

where r is the particle radius, λ is the mean free path of air (67 nm[9]), Δ is the thickness of the transition region (here taken to be 5λ as per Ref. S10), $\xi = r/\lambda$, and f_{ncr} is a function of ξ. The values of the fitting parameters α_f, β, n_r, and r_0 were taken from Ref. S8. We then solve this expression for h, obtaining 1.18 W cm^{-2} K^{-1} for a wire 175 nm in diameter. At 1.8 W cm^{-2} K^{-1}, our experimental value of h is higher by 52%. We attribute the discrepancy to errors in the choice of Δ as 5λ, the maximum value allowed by Ref. S10, and in the fitting parameters taken from Ref. S8, which were determined using samples an order of magnitude larger and smaller in diameter than our nanowires. Heat transfer from solids to air is also strongly affected by environmental conditions such as humidity and air currents, which for our measurements were not likely identical to those of other reports.
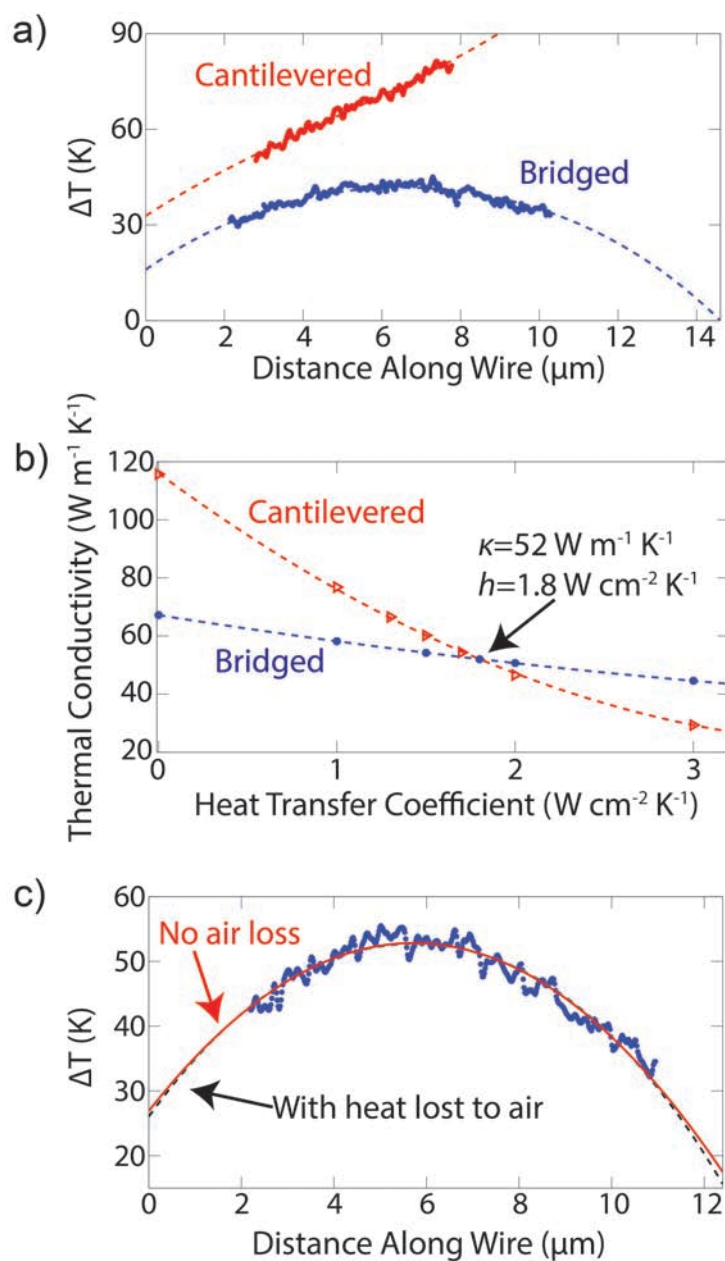
Figure S5: a) Bridged and cantilevered heating profiles for the same wire obtained using the same laser intensity and fit using the correct value of *h*. b) Thermal conductivity calculated using varying values of the heat transfer coefficient for wire 4 in bridged and cantilevered geometry. The intersection of the two curves gives the correct values of the two variables: 52 W m⁻¹ K⁻¹ and 1.8 W cm⁻² K⁻¹, respectively. c) Heating profile for wire 1 collected using 370 µW incident laser intensity and fit to models with and without heat lost to air. The fits are nearly identical in the region of the data. If air conduction is not accounted for, thermal conductivity measured from this profile increases by 19%.

7. Heat losses due to radiation

Power lost to radiation will be proportional to the fourth power of temperature as per the Stefan-Boltzmann law. For a nanowire with the dimensions given in the text at a uniform temperature of 370 K, radiative losses are on the order of nW, three to four orders of magnitude lower than the power absorbed. We therefore consider radiative losses to be negligible.

8. Raman-based stress measurement of laser-heated nanostructures

The application of stress affects the spring constant of the Raman-active phonon mode, downshifting the entire intensity-dependent profile of Raman peak position as well as the room temperature peak position ω_{RT}. With our independent measurement of stress we were able to determine the stress dependence of the Raman shift. Figure S6 shows the change in room temperature peak position with respect to the unstrained nanowire for stresses up to 1.7 GPa. At -3.5 cm^{-1} GPa^{-1}, the slope of the linear fit here is in very good agreement with the relationship between Raman shift and stress along <111> predicted from lattice dynamics[11,12] as well as with experiments on uniaxially stressed bulk Si up to 1.2 GPa in compression[13,14] or 0.15 GPa in tension[15] along <111>. This measurement is the first to be performed on a <111>-oriented Si nanowire, and due to the large range of elastic stresses accessible in Si nanowires, it is the also the highest-stress measurement of this relationship along <111> in Si.
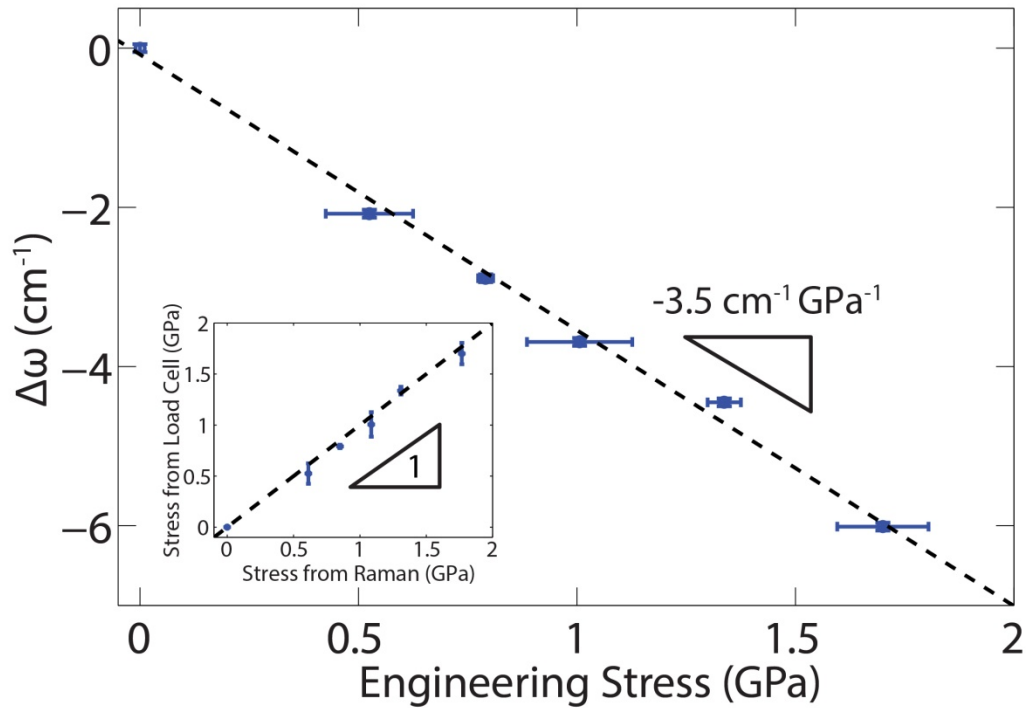
Figure S6: First-order Raman shift of the room temperature peak positions as a function of stress as measured using the MEMS-based load cell. The dotted line is the linear fit to this data and is in very good agreement with reports of this relationship for bulk samples in both tension and compression. Inset: Comparison between stress measured using the MEMS device and stress measured using Raman and the previously-determined relationship between Raman shift and stress for <111> bulk Si in tension (-3.39 cm^{-1} GPa^{-1} [15]). The dashed line represents perfect agreement between our stress measurement and the Raman-based stress measurement.

9. Simulations to determine χ_T dependence on stress

Transverse optical phonon frequencies (corresponding to the Raman shift) of heated, strained silicon were calculated using molecular dynamics (MD)[16] simulations along with lattice dynamics (LD)[17] methods. Unit cells used in the LD calculations were generated using the LAMMPS MD package[18]. First, we considered bulk silicon and used MD simulations with Stillinger-Weber (SW) potential[19] and a time step of 1 fs to relax the crystal structure at 300 K with no external stress present. This was done using a number-, pressure-, and temperature-fixed (NPT) ensemble[20,21] in LAMMPS for 10,000 time steps. We then applied the appropriate external stress and let the system find its equilibrium configuration for another 10,000 time steps. Next, we heated the samples to the target temperature by gradually increasing temperature using a Nose-Hoover thermostat.[22,23] The system was then relaxed for 100,000 time steps to obtain the final strained structure at the desired temperature. The unit cell configuration was then obtained by averaging atom positions over 1,000 time steps after equilibration.

The lattice dynamics technique for this unit cell was then used to derive the dynamical matrix D:[17]

$$D_{3(j-1)+\alpha,3(j'-1)+\alpha'}(\boldsymbol{k}) = \frac{1}{\sqrt{m_j m_{j'}}} \sum_{l'}^{N} \frac{\partial^2 \Phi}{\partial r_\alpha \begin{pmatrix} j \\ 0 \end{pmatrix} \partial r_{\alpha'} \begin{pmatrix} j' \\ l' \end{pmatrix}} \Big|_o \exp i(\boldsymbol{k} \cdot [r\begin{pmatrix} j' \\ l' \end{pmatrix} - r\begin{pmatrix} j \\ 0 \end{pmatrix}]) \qquad (S4)$$

D is a $3n_{cell} \times 3n_{cell}$ matrix where n_{cell} is the number of atoms in one unit cell. In this case, we have the silicon crystal with two atoms per unit cell. α and α' represent any of the three standard Cartesian directions, Φ is the total energy of the crystal obtained from the SW interaction potential, k is the wavevector, m_j is the mass of the jth atom in the unit cell, and $r\begin{pmatrix} p \\ q \end{pmatrix}$ is the position vector of the pth atom in the qth unit cell. Phonon frequencies, including that of the LO branch, were obtained from the eigenvalues of the dynamical matrix. We also performed independent simulations with different initial conditions in order to get a good sampling of the phase space. The average values and the corresponding error bars were then calculated from 10 simulations for each data point.

Figure S7a shows the calculated zone-center optical phonon frequencies at various increments of stress and temperature containing the range of stresses and temperatures used in our experiments. The slope of each fit shown in Figure S7a corresponds to χ_T. Thus, if the slope depends on stress, then so does χ_T. Figure S7b shows the slopes plotted against applied stress, with the error bars the 95% confidence intervals on the fit. It is worth noting that although the exact numbers extracted from these calculations do not precisely match experimental values, we are only concerned with any stress-dependent trends in χ_T since the unstrained experimental value is well known. The results of these calculations exhibit no trend, so we treat χ_T as

unchanging with stress. It is furthermore worth noting that χ_T originates from thermal expansion of the crystal lattice and is therefore intrinsically tied to lattice anharmonicity. Differences in anharmonic behavior at the nanoscale relative to macroscopic behavior would manifest as changes to the elastic behavior at large strains,[24] yet our measurements show both linear elastic response and Young's moduli that agree with bulk values for <111> Si (see Figure S1a and Ref. S1). Thus, our simulations and experiments suggest the value of χ_T for a strained Si nanowire with $d>165$ nm to be the same as that of bulk Si, which is the same as that of unstrained nanowires.[25]
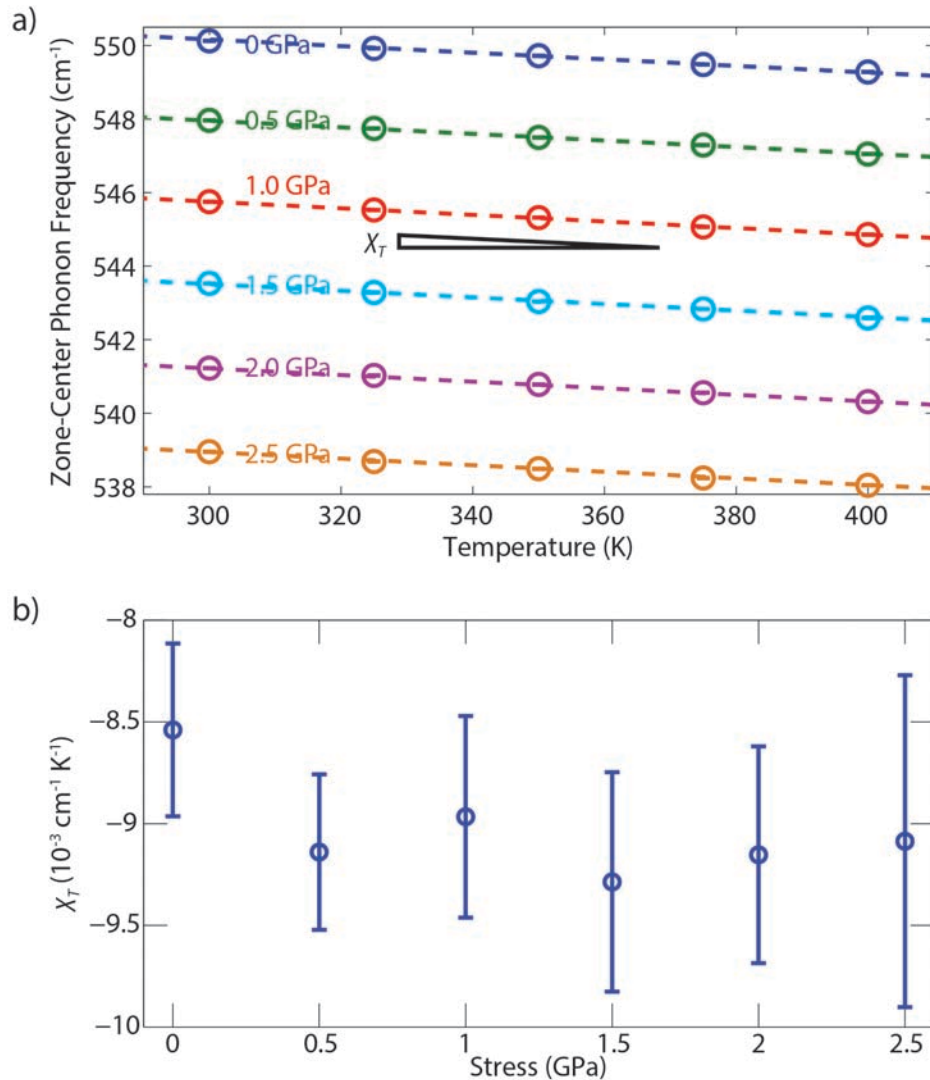

Figure S7: a) Calculated zone center longitudinal optical phonon frequency at various temperatures and stresses, corresponding to Raman shift for the first-order Si peak near 520 cm^{-1}. The slope of the fit shown is the relationship between Raman shift and temperature for a given stress ($\chi_T(\sigma)$). b) $\chi_T(\sigma)$ for $\sigma=0$ to 2.5 GPa. The error bars are the 95% confidence intervals on the slope of the fits to the data shown in (a).

10. Approximate method based on thermal circuits and the total thermal resistance

Power transferred to the surrounding air may be accounted for by treating the air as a thermal resistor in parallel with the nanowire-contact series (see Figure S8a). Since the loss from any point along the nanowire depends on the temperature at that point, the total loss depends on the full temperature profile in the nanowire for any given laser position s. We approximate this profile by solving the heat equation with no losses to air ($h=0$), no contact resistance ($R_{c,l}=R_{c,r}=0$), and an infinitely narrow Gaussian heat source ($w=0$). The solution gives the profile shown in Figure S8b, which is linear between the laser spot and each heat sink. By integrating the triangular profile we arrive at a simple expression for the temperature rise as a function of laser position:

$$\Delta T(s) = R_{system}P = \left(\frac{1}{\frac{s}{A\kappa} + R_{c,l}} + \frac{1}{\frac{L-s}{A\kappa} + R_{c,r}} + \frac{hCL}{2} \right)^{-1} P \qquad (S5)$$

Fitting heating profiles to equation S5 yields curves and thermal conductivities in excellent agreement with equation 2, as can be seen in Figure S8c.

An alternative means of determining thermal conductivity is using equation 1 from the main text, which gives the total thermal resistance of the system, R_{system}, as a function of the slope of the fit to the plot of temperature against laser power. We may then solve equation S5 for κ, substituting the calculated value of R_{system} as well as the previously-fitted values of h, $R_{c,l}$ and $R_{c,r}$. We note that applying this procedure to equation 1 is mathematically unwieldy, necessitating the good approximation explicated here. The thermal conductivities calculated using this approximate, slope-based method are in excellent agreement with those calculated using the exact method, as can be seen in main text Figure 3.
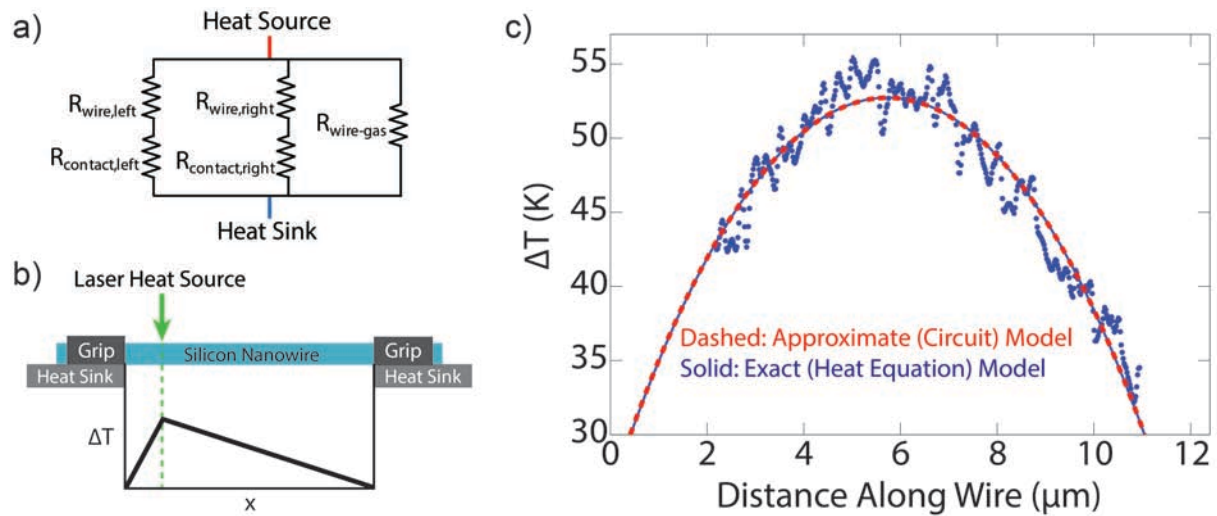
Figure S8: a) Schematic of thermal resistor model. The nanowire-contact series on either side of the laser are in parallel with each other as well as the nanowire-gas interface. b) Approximate instantaneous temperature profile in the nanowire used to calculate the thermal resistance of the nanowire-gas interface leg of the circuit. c) A heating profile for wire 1 fit to the exact model (equation 2) and the approximate model (equation S5). The fits are nearly identical and yield thermal conductivities within 1 W m^{-1} K^{-1} of each other.

11. Errors due to thermal expansion

Assuming the linear coefficient of thermal expansion for silicon is 2×10^{-6} K^{-1} and our temperature excursions are no more than 80 K, the maximum thermal expansion we would expect would be approximately 1 nm. Since our load cell has stiffness 44 N m^{-1}, this corresponds to 44 nN or 2 MPa of stress in the nanowire, corresponding to an error in the Raman shift of 0.007 cm^{-1}, a negligible error.

12. Correction for actuator heating

For strained increments, there is slight heating of one side from the thermal actuator, yielding a temperature difference between the grips of no more than 40 K. To correct for this, a scan was made at power low enough to yield laser-induced heating below the noise floor of our temperature measurement (about 4 K). The slope of this curve, an example of which is shown in Figure S9a, was taken to be the gradient due to temperature and removed from the strained plots. An example of an uncorrected strained plot and the same data corrected for the temperature gradient and fitted to equation 2 is shown in Figure S9b.
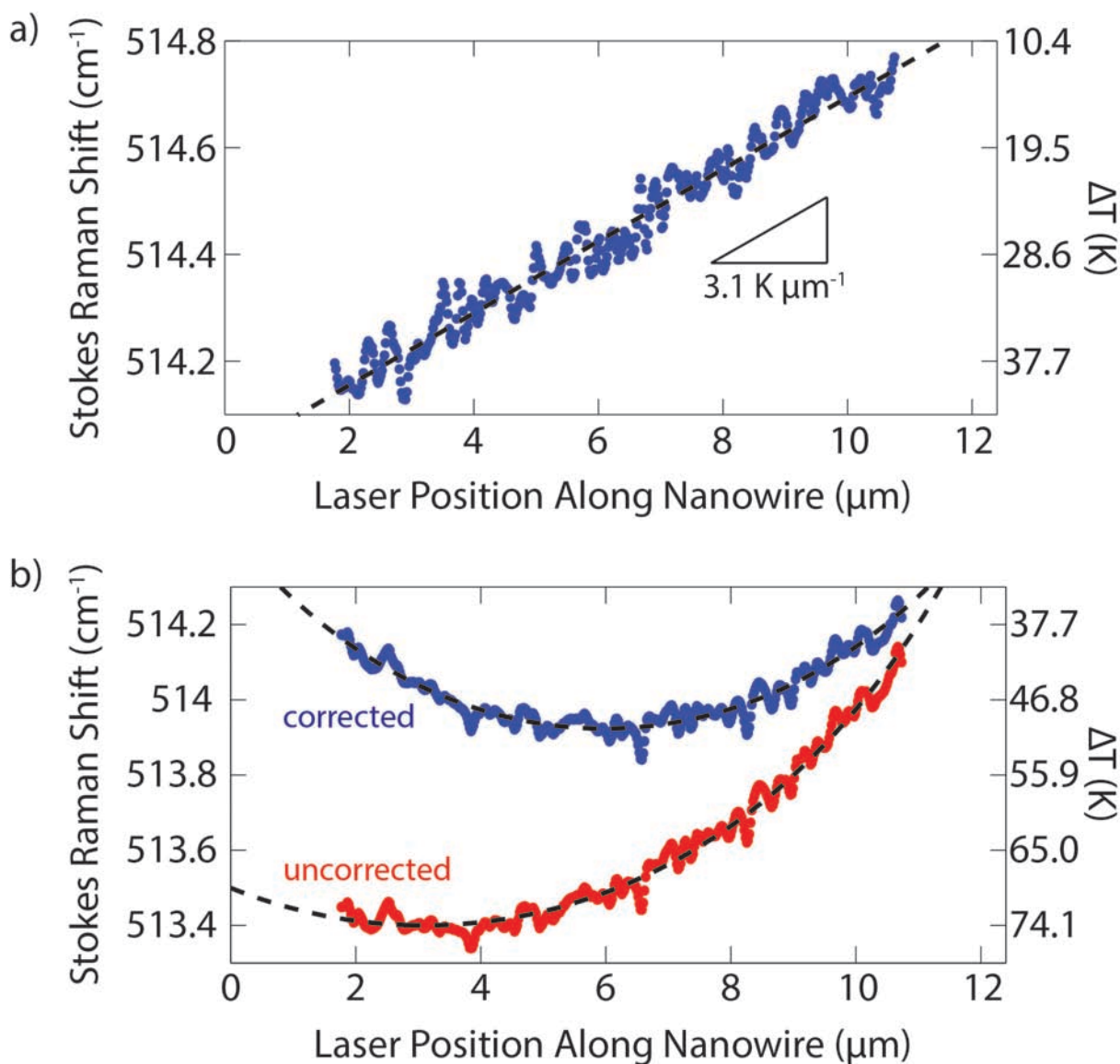
Figure S9: a) Peak position and temperature profile at 1.7 GPa obtained using applied laser power 61 μW, low enough that the laser-induced heating was below the resolution of our measurement. The slope of the linear fit corresponds to a temperature gradient across the wire of 3.1 K μm^{-1} and was taken to be entirely due to heating from the actuator. b) Peak position and temperature profiles with the corresponding fits at 1.7 GPa obtained using applied laser power 0.22 mW, uncorrected and corrected for the slope shown in (a).

13. Ion irradiation

All nanowires were irradiated with Ga^+ ions inside a dual-beam scanning electron and focused ion beam (FIB) microscope at 30 kV accelerating voltage and 20,000× magnification. Ion bombardment occurred at normal incidence to the surface of the nanowire without rotation about the nanowire growth axis. Dwell times were set so that the fluence was 4 ions nm^{-2}. Although the precise temperature in the immediate sample environment during irradiation was unknown, the microscope chamber and stage were held at room temperature.

14. Estimates of measurement uncertainty

Deflection of the load cell (proportional to stress) is measured using digital image correlation (DIC) both on loading and unloading, such that we have two measurements of stress for each increment. We observe no trends in the difference between the loading and unloading stresses with load, and we observe no systematic difference that would indicate that the wire or contacts plastically deform during collection of Raman data, so the difference between the loading and unloading stresses was taken to be the error on our measurements of stress. The mean difference across all stress measurements was 6 MPa.

We estimate the error on our temperature measurement by examining the 95% confidence intervals on the fits to each spectrum. The Lorentzian + Gaussian fits yield mean error on the peak position values conservatively below 0.05 cm^{-1}. The 95% confidence error on the linear fit which yields the room temperature peak position ω_{RT} is also <0.05 cm^{-1}, so the error on $\Delta\omega$ is therefore <0.1 cm^{-1}. The error on our determination of temperature is therefore <4 K.

Thermal conductivity and contact resistance were measured from the temperature profiles with fitted curvature greater than 2.5 K μm^{-2}, which typically yielded 95% confidence intervals on the fitting parameters within 20% of the mean values. The residuals of these fits, shown in Figure S10, are consistent with the error on the peak fits. Between 10 and 20 of the temperature profiles at each stress increment met this requirement; the error bars on Figure 3 represent the standard deviation of the resulting values of thermal conductivity using these profiles.
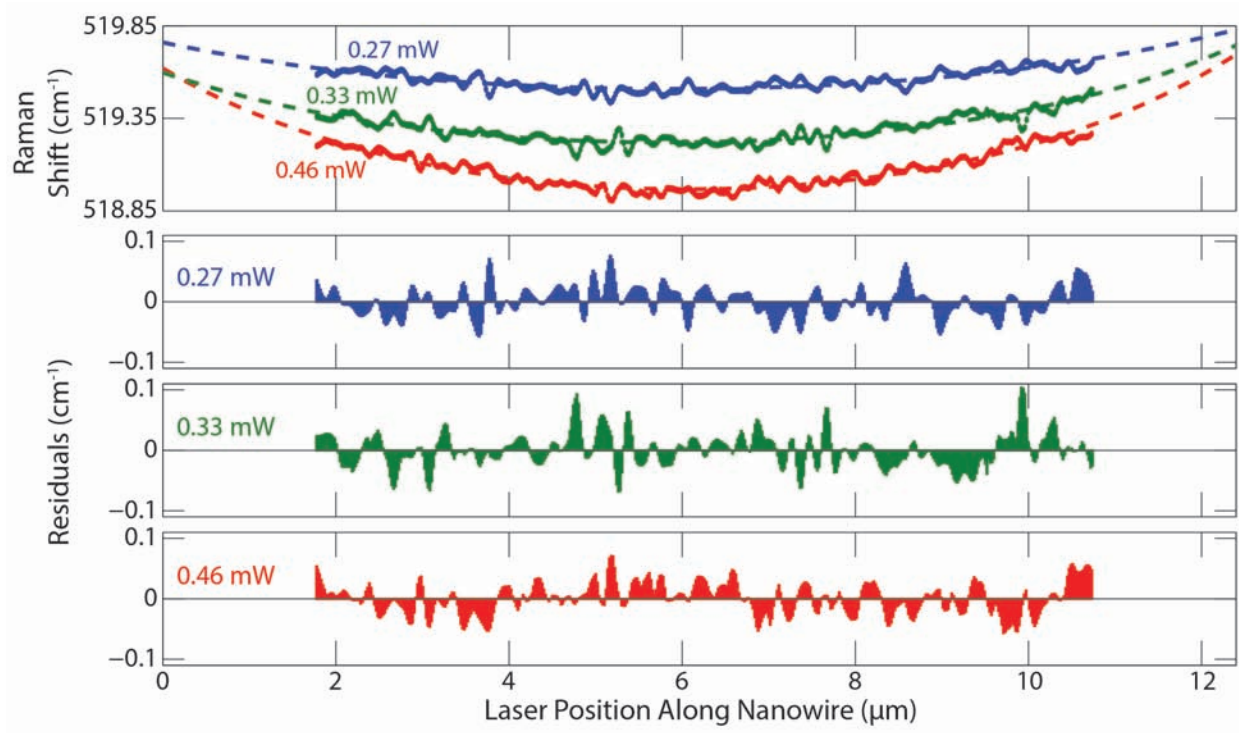
Figure S10: The fits shown in Figure 2a with accompanying residuals. The RMS values of the residuals for 0.27, 0.33, and 0.46 mW are 0.024, 0.028, and 0.025 cm^{-1}, respectively.

Supplementary References

(S1)   Murphy, K. F.; Chen, L. Y.; Gianola, D. S. Effect of Organometallic Clamp Properties on the Apparent Diversity of Tensile Response of Nanowires. *Nanotechnology* **2013**, *24*, 235704.

(S2)   Sulfridge, M.; Saif, T.; Miller, N.; O'Hara, K. Optical Actuation of a Bistable MEMS. *J. Microelectromechanical Syst.* **2002**, *11*, 574–583.

(S3)   Sampathkumar, A.; Murray, T. W.; Ekinci, K. L. Photothermal Operation of High Frequency Nanoelectromechanical Systems. *Appl. Phys. Lett.* **2006**, *88*, 223104.

(S4)   Kerker, M. *The Scattering of Light and Other Electromagnetic Radiation*; Academic Press: New York, 1969.

(S5)   Palik, E. D. *Handbook of Optical Constants of Solids*; Academic Press, 1996.

(S6)   Incropera, F. P.; DeWitt, D. P. *Introduction to Heat Transfer*; 3rd ed.; John Wiley & Sons, Inc., 1996.

(S7)   Cheng, C.; Fan, W.; Cao, J.; Ryu, S.-G.; Ji, J.; Grigoropoulos, C. P.; Wu, J. Heat Transfer Across the Interface Between Nanoscale Solids and Gas. *ACS Nano* **2011**, *5*, 10102–10107.

(S8)   Wang, H.-D.; Liu, J.-H.; Zhang, X.; Li, T.-Y.; Zhang, R.-F.; Wei, F. Heat Transfer Between an Individual Carbon Nanotube and Gas Environment in a Wide Knudsen Number Regime. *J. Nanomater.* **2013**, *2013*, 1–7.

(S9)   Jennings, S. . The Mean Free Path in Air. *J. Aerosol Sci.* **1988**, *19*, 159–166.

(S10)   Klein, H. H.; Karni, J.; Ben-Zvi, R.; Bertocchi, R. Heat Transfer in a Directly Irradiated Solar Receiver/reactor for Solid–gas Reactions. *Sol. Energy* **2007**, *81*, 1227–1239.

(S11)   Ganesan, S.; Maradudin, A. A.; Oitmaa, J. A Lattice Theory of Morphic Effects in Crystals of the Diamond Structure. *Ann. Phys. (N. Y).* **1970**, *56*, 556–594.

(S12)   De Wolf, I.; Maes, H. E.; Jones, S. K. Stress Measurements in Silicon Devices through Raman Spectroscopy: Bridging the Gap Between Theory and Experiment. *J. Appl. Phys.* **1996**, *79*, 7148–7156.

(S13)   Anastassakis, E.; Pinczuk, A.; Burstein, E.; Pollak, F. H.; Cardona, M. Effect of Static Uniaxial Stress on the Raman Spectrum of Silicon. *Solid State Commun.* **1970**, *8*, 133–138.

(S14)   Anastassakis, E.; Cantarero, A.; Cardona, M. Piezo-Raman Measurements and Anharmonic Parameters in Silicon and Diamond. *Phys. Rev. B* **1990**, *41*, 7529–7535.

(S15) Peng, C.-Y.; Huang, C.-F.; Fu, Y.-C.; Yang, Y.-H.; Lai, C.-Y.; Chang, S.-T.; Liu, C. W. Comprehensive Study of the Raman Shifts of Strained Silicon and Germanium. *J. Appl. Phys.* **2009**, *105*, 083537.

(S16) Allen, M. P.; Tildesley, D. J. *Computer Simulation of Liquids*; Oxford Science Publication, 2001.

(S17) Dove, M. T. *Introduction to Lattice Dynamics*; Cambridge University Press, 1993.

(S18) Plimpton, S. Fast Parallel Algorithms for Short-Range Molecular Dynamics. *J. Comput. Phys.* **1995**, *117*, 1–19.

(S19) Stillinger, F. H.; Weber, T. A. Computer Simulation of Local Order in Condensed Phases of Silicon. *Phys. Rev. B* **1985**, *31*, 5262–5271.

(S20) Shinoda, W.; Shiga, M.; Mikami, M. Rapid Estimation of Elastic Constants by Molecular Dynamics Simulation Under Constant Stress. *Phys. Rev. B* **2004**, *69*, 134103.

(S21) Parrinello, M.; Rahman, A. Polymorphic Transitions in Single Crystals: A New Molecular Dynamics Method. *J. Appl. Phys.* **1981**, *52*, 7182–7190.

(S22) Nosé, S. A Unified Formulation of the Constant Temperature Molecular Dynamics Methods. *J. Chem. Phys.* **1984**, *81*, 511–519.

(S23) Hoover, W. G. Canonical Dynamics: Equilibrium Phase-Space Distributions. *Phys. Rev. A* **1985**, *31*, 1695–1697.

(S24) Chen, L. Y.; Richter, G.; Sullivan, J. P.; Gianola, D. S. Lattice Anharmonicity in Defect-Free Pd Nanowhiskers. *Phys. Rev. Lett.* **2012**, *109*, 125503.

(S25) Doerk, G. S.; Carraro, C.; Maboudian, R. Temperature Dependence of Raman Spectra for Individual Silicon Nanowires. *Phys. Rev. B* **2009**, *80*, 073306.